Am J Cancer Res 2024;14(1):253-273
www.ajcr.us /ISSN:2156-6976/ajcr0153559

Original Article

A prognostic metabolism-related gene signature associated with the tumor immune microenvironment in neuroblastoma

Xin Yu[1,2,3*], Chao Xu[1,2,3,4*], Yiping Zou[1,2,3], Weishuai Liu[1,2,3], Yongjie Xie[1,2,3], Chao Wu[1,2,3]

[1]Tianjin Medical University Cancer Institute and Hospital, National Clinical Research Center for Cancer, Tianjin, China; [2]Tianjin's Clinical Research Center for Cancer, Tianjin, China; [3]Key Laboratory of Cancer Immunology and Biotherapy, Tianjin, China; [4]National Clinical Research Center for Cancer, Tianjin Cancer Hospital Airport Hospital, Tianjin, China. [*]Equal contributors.

Received September 21, 2023; Accepted January 15, 2024; Epub January 15, 2024; Published January 30, 2024

Abstract: Neuroblastoma (NB) is the most prevalent malignant solid tumor in children. Tumor metabolism, including lipid, amino acid, and glucose metabolism, is intricately linked to the genesis and progression of tumors. This study aimed to establish a prognostic gene signature for NB patients, based on metabolism-related genes, and to investigate a treatment approach that could enhance the survival rate of high-risk NB patients. From the NB dataset GSE49710, we identified metabolism-related gene markers utilizing the "limma" R package and univariate Cox analysis combined with least absolute shrinkage and selection operator (LASSO) regression analysis. We explored the correlation between these gene markers and the overall survival of NB patients. Gene set enrichment analysis (GSEA) and single-sample GSEA algorithms were used to assess the differences in metabolism and immune status. Furthermore, we examined the association between metabolic subgroups and drug responsiveness. Concurrently, data downloaded from TARGET and MTAB were used for external verification. Using multicolor immunofluorescence and immunohistochemistry, we investigated the relationship between the lipid metabolism-related gene ELOVL6 with both the International Neuroblastoma Staging System classification of NB and survival rate. Finally, we explored the effect of high ELOVL6 expression on the immune microenvironment in NB using flow cytometry. We identified an eight-gene signature comprising metabolism-related genes in NB: ELOVL6, OSBPL9, RPL27A, HSD17B3, ACHE, AKR1C1, PIK3R1, and EPHX2. This panel effectively predicted disease-free survival, and was validated using an internal dataset from GSE49710 and two external datasets from the TARGET and MTAB databases. Moreover, our findings confirmed that ELOVL6 fosters an immunosuppressive microenvironment and contributes to the malignant progression in NB. The eight-gene signature is significant in predicting the prognosis of NB, effectively classifying patients into high- and low-risk groups. This classification may guide the development of innovative treatment strategies for these patients. Notably, the signature gene ELOVL6 markedly encourages an immunosuppressive microenvironment and malignant progression in NB.

Keywords: Neuroblastoma, metabolism-related genes, prognostic model, ELOVL6, immune microenvironment

Introduction

Neuroblastoma (NB), the most common extracranial solid tumor in children, is an embryonal tumor originating from sympathetic neural progenitor cells and accounts for at least 10% of childhood cancer deaths [1]. Treatment options for NB, influenced by factors such as age, *MYCN* amplification, chromosomal aberrations, history of metastases, etc., include chemotherapy, surgical resection, myeloablation with autologous stem cell transplantation, radiation therapy, and immunotherapy [2]. Commonly used chemotherapeutic agents for NB include cyclophosphamide, cisplatin, doxorubicin, etoposide, carboplatin, and vincristine [3]. The survival rate of NB patients largely depends on age at diagnosis, stage of disease, and pathophysiology. Although the disease is self-limiting, its prognosis remains poor with a high recurrence rate in high-risk patients [2]. Therefore, identifying new therapeutic targets and developing targeted therapeutic strategies for NB are urgently needed.

https://doi.org/10.62347/IDXM4018

A hallmark of cancer is the reprogramming of energy metabolism to support growth and survival in adverse conditions, contributing to cancer progression [4]. Moreover, in the tumor microenvironment (TME), various metabolites affect the differentiation and effector functions of immune cells [5]. The immune response is closely linked to substantial changes in tissue metabolism. Aerobic glycolysis and the subsequent acidification of the TME significantly influence T cell-mediated anti-tumor immune responses and the function of tumor-infiltrating myeloid cells [6]. For instance, lactate produced by tumor cells can promote tumorigenesis by inducing inflammation mediated through interleukins-23 and -17 [7]. Tumor-infiltrating myeloid cells, such as myeloid-derived suppressor cells (MDSCs), dendritic cells, and tumor-associated macrophages, undergo metabolic reprogramming in response to abnormal accumulations of lipids, including short- and long-chain fatty acids and cholesterol [8]. The impact of metabolic reprogramming on NB progression and its underlying mechanisms remains to be explored.

This study aimed to investigate the correlation between cellular metabolism and NB progression. Gene expression data from Gene Expression Omnibus (GEO) were used to construct NB molecular subtypes based on energy metabolism-related genes. We then evaluated the association between these molecular subtypes and patient prognosis. Through differential expression analysis and least absolute shrinkage and selection operator (LASSO)-Cox regression, eight genes were finally selected from the 222 differentially expressed genes (DEGs) to construct a prognostic risk model. This model independently evaluates the prognosis of NB patients and has been validated by internal GEO, Therapeutically Applicable Research to Generate Effective Treatments (TARGET), and MTAB external validation cohorts. Additionally, we assessed the model's clinical relevance, metabolic significance, immune landscape, and implications for immune pharmaceutical therapy. Among the eight metabolism-related genes, *ELOVL6* had the highest coefficient value. Through a series of *in vitro* and *in vivo* experiments, we demonstrated that high expression of *ELOVL6* was closely associated with poor prognosis and an immunosuppressive TME in NB, further corroborating the predictive ability of this prognostic model.

Methods

Data collection and preprocessing

Expression profiles and associated clinical information of NB samples were downloaded from GEO (accession: GSE49710) [9], ArrayExpress (accession: E-MTAB-8248) (35100718), and the TARGET cohort of NB patients in the University of California Santa Cruz Xena platform (https://xenabrowser.net/). A total of 871 samples were included in this study. Within the GSE49710 cohort, 70% were designated as the training group and the remaining 30% as the internal validation group. The E-MTAB-8248 and the TARGET cohorts served as the external validation groups. For further analysis, the expression profile data in the TARGET cohort was transformed from fragments per kilobase of transcript per million fragments mapped to transcripts per kilobase million. Metabolism-related genes were obtained from the Molecular Signatures Database (MSigDB; https://www.gsea-msigdb.org/gsea/msigdb) (Table S1).

Consensus clustering analysis

To uncover expression patterns, unsupervised consensus clustering analysis was performed based on prognostic metabolism-related genes in the GSE49710 datasets using the "Consensus Cluster Plus" R package and the "k-means" method. The repetition number was set to 1,000 to ensure stability [10]. Principal component analysis (PCA) was conducted using the "scatterplot3d" package to investigate the distribution between distinct clusters.

Gene set variation analysis (GSVA)

GSVA was carried out to determine the enrichment scores and pathway activity in the hallmark gene sets and Kyoto Encyclopedia of Genes and Genomes (KEGG) pathways. The gene sets used in GSVA were downloaded from MSigDB.

DEGs analysis

The DEGs between different metabolism-related clusters were identified using the "limma" R

package with the following criteria: $|\log_2(\text{fold-change})| \geq 0.58$ and adjusted p-value < 0.05. The intersection of DEGs and prognostic metabolism-related genes yielded metabolism-related DEGs for constructing the risk signature.

Construction and validation of the metabolism-related risk signature

LASSO-Cox regression analysis identified signature genes and their corresponding regression coefficients. Risk scores were calculated by multiplying the expression value of each gene with its corresponding regression coefficient. Samples were divided into high- and low-risk groups based on median scores. Kaplan-Meier survival curves, compared using the log-rank test, evaluated the prognostic capability of the metabolism-related risk signature. The accuracy of the risk signature for 1-, 2-, 3-, and 5-year survival rates was assessed by calculating the area under the curve (AUC) of receiver operating characteristic curves using the "survivalROC" R package. PCA was performed to distinguish different risk groups using the "ggplot2" R package.

Independent prognostic analysis

The "survival" and "rms" R packages were respectively used to determine the independent prognostic value of the risk signature through univariate and multivariate Cox regression analysis, and construct a nomogram for predicting the 3-year and 5-year overall survival.

Gene set enrichment analysis (GSEA)

GSEA was performed to identify pathways enriched in the low- and high-risk groups, and to reveal the differences in their biological functions. The gene sets for GSEA were downloaded from MSigDB.

Immune infiltration analysis

The infiltration level of 30 immune cell types was evaluated and compared between the low- and high-risk groups using single-sample GSEA [11, 12]. The immune and stromal cell infiltration levels [13] were determined using the ESTIMATE algorithm (The Estimation of Stromal and Immune cells in Malignant Tumor tissues using Expression data).

Drug sensitivity analysis

A series of drug sensitivities were predicted using Ridge's regression in the "pRRophetic" R package (25229481). Half-maximal inhibitory concentrations were calculated and comparisons were made between the low- and high-risk groups.

Clinical samples

A total of 78 NB tumor tissue samples were collected from January 2015 to January 2022 at the Institute of Oncology and Hospital of Tianjin Medical University. Clinical characteristics of all patients included in this study are shown in Table S2. All procedures for this study were authorized by the Research Ethics Committee of the Institute of Oncology and Hospital of Tianjin Medical University and conducted in accordance with the Code of Ethics of the World Medical Association (the Declaration of Helsinki). Fully informed consent was obtained for all clinical samples.

Immunohistochemistry (IHC) and multiplex fluorescent IHC

IHC analysis of NB tissue for ELOVL6 expression was performed using a DAB substrate kit (Maxin). The score was determined based on staining intensity (0: negative, 1: low, 2: medium, 3: high) and extent (0: 0%, 1: 1-25%, 2: 26-50%, 3: 51-75%, 4: 76-100%). Five random fields were evaluated under a light microscope. Scores were determined by two independent pathologists, blinded to patients' clinical features and outcomes. The final staining scores were determined by multiplying the staining intensity scores by the staining extent scores. The final score ranged from 0 to 12. For multiplex fluorescent IHC, stained tissues were scanned and captured using a Vectra Polaris system (PerkinElmer). Captured images were analyzed using the inForm cell analysis software (PerkinElmer).

Cell culture

Mouse NB cell lines 9464D and 975A2 were cultured in high-glucose Dulbecco's Modified Eagle Medium (DMEM, Gibco) supplemented with 10% fetal bovine serum (BI) and 0.1% penicillin-streptomycin solution (Gibco). The human NB cell line SK-N-AS was cultured in high-glucose DMEM:F12 (Gibco) supplemented with

10% fetal bovine serum (BI) and 0.1% penicillin-streptomycin solution (Gibco). The human NB cell line SK-N-BE2 was cultured in high-sugar DMEM:F12 (Gibco) supplemented with penicillin-streptomycin solution (Gibco) at 37°C and 5% CO_2.

Western blot

Total protein was extracted from the stable cell lines ELOVL6-OE/ELOVL6-Vector SK-N-AS and SK-N-BE2 using the radioimmunoprecipitation assay protein lysis kit containing protease and phosphatase inhibitors. Protein concentrations were uniformly quantified using the bicinchoninic acid assay protein kit. Each protein sample (20 μg) was resolved on 10-12% sodium dodecyl sulfate polyacrylamide gels and electro-transferred onto 0.2-μm polyvinylidene fluoride membranes (Millipore, Billerica, MA). The membranes were incubated with 5% skimmed milk for 1 h at room temperature, probed with the corresponding primary antibodies overnight at 4°C (Table S3), washed thrice with phosphate-buffered saline (PBS) for 3 min each, incubated with anti-rabbit or anti-mouse immunoglobulin G (1:5000) for 1 h at room temperature, and washed thrice with PBS for 2 min each. Stained bands were visualized using the GelView 6000 Plus system and analyzed using ImageJ.

RNA extraction and quantitative RT-PCR analysis

Total RNA was isolated using the RNeasy mini kit (QIAGEN) according to the manufacturer's instructions. RNA was quantified by UV spectrophotometry. In brief, the cells were lysed with the Qiazol reagent for at least 5 minutes at room temperature and then chloroform was added. The aqueous phase was collected, mixed with ethanol and loaded onto RNeasy Mini columns after centrifugation at 12,000 × g for 15 min at 4°C. After sequential washing with RWT and RPE buffer, the RNA was eluted from the membrane with RNase-free water and recovered by centrifugation. For mRNA expression analysis, 200-500 ng of RNA was reverse transcribed to cDNA using the QuantiTect Reverse Transcription Kit (QIAGEN). Quantitative real-time PCR was then performed using Maxima SYBR green qPCR master mix (Thermo Fisher Scientific) on a QuantStudio 7 Flex PCR system (Thermo Fisher Scientific) with 0.5 mL of diluted cDNA (2.5-fold dilution) utilizing GAPDH as an endogenous control. Each sample was run in triplicate. The following lists the primers used for RT-qPCR analysis: GAPDH-F: CCTGCACCACCAACTGCTTA; GAPDH-R: TCATGAGCCCTTCCACAATG; ELOVL6-F: CAGGGAGGAAGGGCTATGGGCAG; ELOVL6-R: CGAACAGGGAGGGAGGCGAACA.

Animal experiments

Female C57BL/6 mice (6-8-week-old, 18-20 g) were obtained from Beijing Vital River Laboratory Animal Technology Co. (Beijing, China) and bred in a pathogen-free environment. All animal experiments were performed in accordance with the Guide for the Care and Use of Laboratory Animals and were approved by the Institutional Animal Care and Use Committee of Tianjin Medical University Cancer Institute and Hospital. To evaluate the impact of *ELOVL6* in the NB xenograft model, the stably expressing ELOVL6 OE/Vector 9464D cells or ELOVL6 sh/SC 975A2 cells (1.5×10^6 per 100 μL of PBS per mouse) were injected into the axillae of mice. After tumor implantation, the tumor volume was measured every 3 days using the following formula: tumor volume = (length × $[width]^2$)/2. Pose-euthanasia, tumors were harvested and weighed for further analysis. Fresh tumor tissue was used for flow cytometry.

Flow cytometry

Harvested mouse NB tumors were processed into single-cell suspensions at a cell density of 10^5-10^7/mL for fluorescent or immunofluorescent labelling. Cells were stained with antibodies for 30 min at 4°C (Table S3), while the control samples were treated with corresponding isotype controls. Data were collected using a CytoFLEX LX flow cytometer (Beckman, USA) and processed using FlowJo.

Cell proliferation assay

Stable cell lines ELOVL6/Vector SK-N-AS/SK-N-BE2 were transfected in their logarithmic growth phase, further cultured in 96-well plates for 24, 48, or 72 h, and incubated with CCK-8 reagent (Solarbio, China) for 3 h. The optical density values were measured using a microplate reader (Biotek Instruments Inc., USA), and

proliferation curves were plotted using GraphPad Prism 8.0.

Lipid peroxidation malondialdehyde (MDA) assay

The Lipid Peroxidation MDA Assay Kit (Beyotime, S0131S) was used according to the manufacturer's instructions to assay the relative MDA concentration in cell lysates. Briefly, stable cell lines were lysed using Western blot lysis buffer, and the supernatants were extracted by centrifugation at 10,000-12,000 g for 10 min. Protein concentrations were determined using the BCA protein concentration assay kit (THERMO) to determine the MDA content per unit protein weight in tissue or cells. Obtained supernatants (100 μL) were mixed with 200 μL of MDA working solution and incubated at 100°C for 15 min. Samples were cooled to room temperature and the absorbance of each mixture was measured at 532 nm.

Glutathione reductase assay

Glutathione reductase activity in the cell lysates was assayed using the Glutathione Reductase Assay Kit with DTNB (Beyotime, S0055), according to the manufacturer's protocol. Briefly, stable cell lines were lysed using Western blot lysis buffer and the supernatants were isolated by centrifugation at 10,000-12,000 g for 10 min. Supernatants were mixed with the Glutathione Reductase assay working solution and the absorbance at 412 nm was determined every 2 min at 25°C using an enzyme marker. The results were calculated according to the manufacturer's protocol.

Glutathione peroxidase assay

Glutathione peroxidase activity in the cell lysates was measured using the Total Glutathione Peroxidase Assay Kit with NADPH (Beyotime, S0058), according to the manufacturer's protocol. Briefly, stable cell lines were lysed using Western blot lysis buffer and the supernatants were isolated by centrifugation at 10,000-12,000 g for 10 min. Supernatants were mixed with the Glutathione Peroxidase working solution and incubated for 15 min at room temperature. The absorbance at 340 nm was measured continuously for 5 min or automatically in 1-min intervals. The results were calculated according to the manufacturer's protocol.

Iron assay

Levels of intracellular ferrous ions (Fe^{2+}) and the total iron content were measured using the Iron Assay Kit (ab83366, Abcam), according to the manufacturer's instructions. Stably transfected NB cells were seeded in 10-cm plates, treated with erastin or dimethyl sulfoxide for 48 h, harvested, washed with ice-cold PBS, and resuspended on ice in 5 × volume of iron assay buffer. Supernatants were isolated by centrifugation at 4°C for 10 min at 13,000 g, mixed with iron-reducing agent, incubated for 30 minutes at room temperature, then combined with 100 μL of the iron probe, and incubated for 1 hour in the dark at room temperature. Absorbance at 593 nm was measured immediately using an enzyme marker.

Statistical analysis

All statistical analyses were conducted using software (version 4.1.2). Continuous variables were compared using the Mann-Whitney Wilcoxon test or the Kruskal-Wallis test. Categorical variables were compared using the Pearson chi-squared test. The log-rank test was applied for comparing the prognoses in risk groups. A p-value < 0.05 (two-tailed) was considered statistically significant.

Results

Identification and characteristics of metabolism-related clusters

The flow chart for this study is presented in **Figure 1**. From the GSE49710 dataset, we retrieved 1216 metabolism-related genes, among which 802 were identified as prognostic genes (**Figure 2A**). Enrichment analyses were performed to explore the biological functions of these prognostic metabolism-related genes. Gene Ontology enrichment analysis revealed significant enrichment of these genes in carbon metabolism, glycerophospholipid metabolism, biosynthesis of amino acids, and fatty acid metabolism (**Figure 2B**). Similarly, KEGG enrichment analysis demonstrated significant enrichment in fatty acid, glycerolipid, and phospholipid metabolism, underscoring the pivotal role of lipid metabolism in NB development and progression (**Figure 2B**).

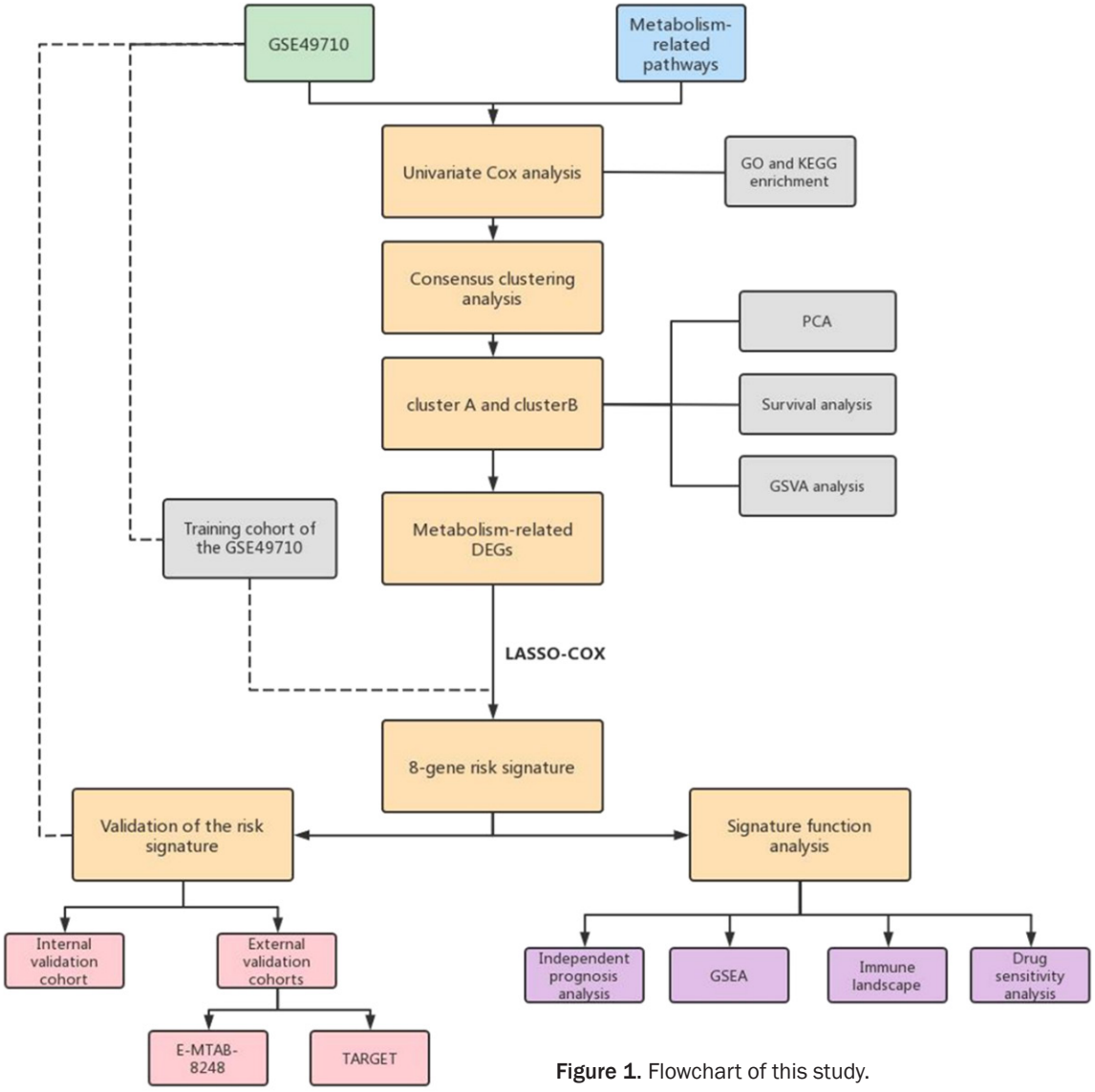

Figure 1. Flowchart of this study.

Given the complexity of metabolic processes in NB, consensus clustering analysis was performed to discern different metabolic patterns. Based on the prognostic metabolism-related genes, we identified two distinct metabolism-mediated clusters in the GSE49710 dataset (**Figures 2C**, S1), which were clearly distinguishable by PCA (**Figure 2D**). Survival analysis revealed that cluster A had a significantly better prognosis compared to cluster B ($P < 0.001$, **Figure 2E**). Furthermore, we performed GSVA to elucidate the differences in metabolic processes between these clusters. Cluster B was enriched in glycine, serine, and threonine metabolism, alanine, aspartate, glutamate metabolism, and arginine and proline metabolism (**Figure 2F**), whereas cluster A was enriched in taurine, hypotaurine, and arachidonic acid metabolism. Additionally, we observed differences in biological functions between the clusters using hallmark gene sets, with cluster B enriched in MYC targets and DNA repair pathways, while apoptosis and p53 pathways were activated in cluster A (**Figure 2G**).

Construction of the metabolism-related risk signature

Given the considerable prognostic value of the metabolism-mediated clusters, we constructed a metabolism-related risk signature to predict NB prognosis. Firstly, the two clusters underwent differential gene expression analysis. We identified 222 metabolism-related DEGs as

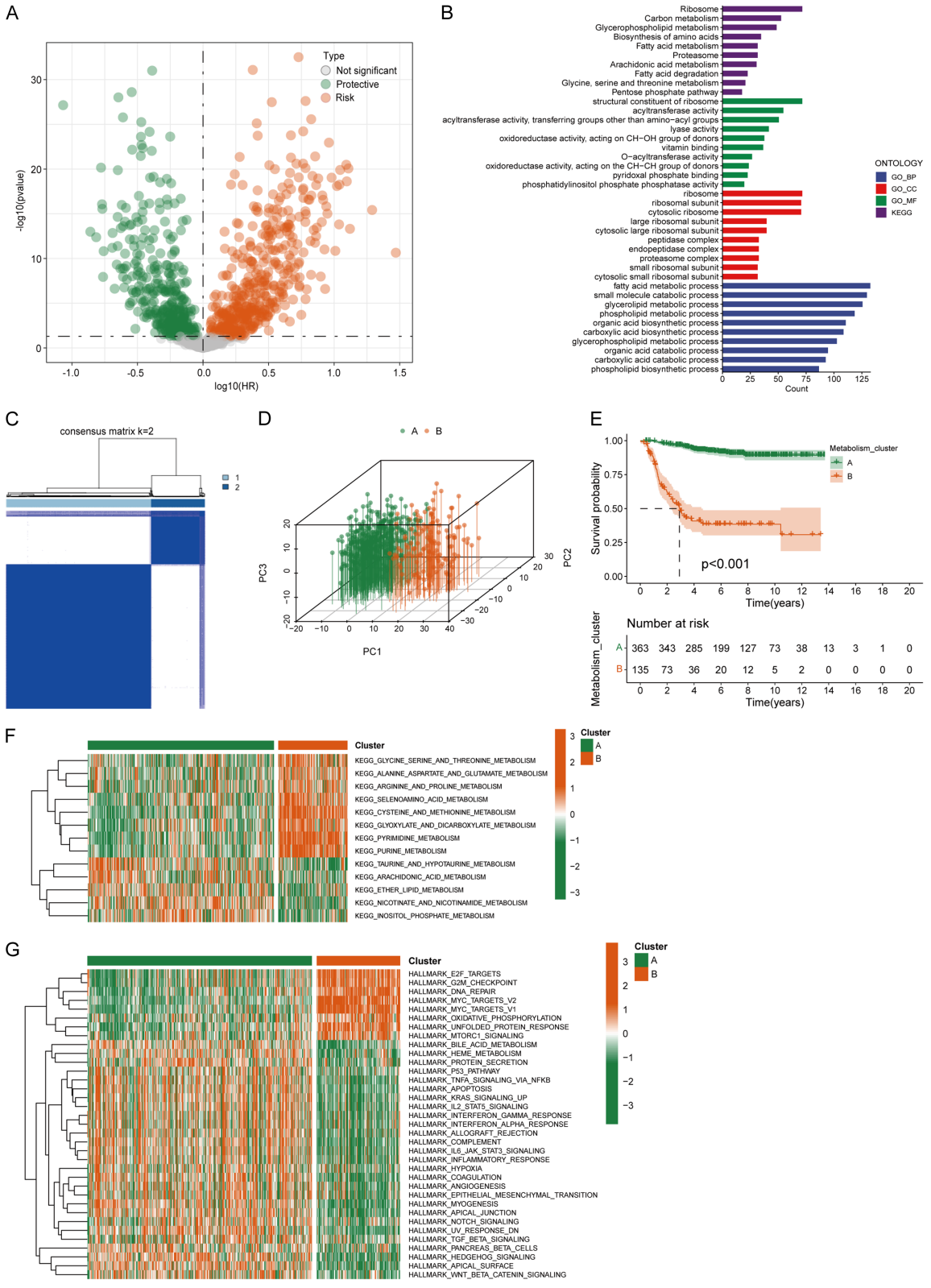

Figure 2. Identification of metabolism-related clusters in the GSE49710 dataset. A. Volcano plot of prognostic metabolism-related genes in the GSE49710 dataset. The orange dots represent risk genes and the green dots represent protective genes with statistical significance. The gray dots represent nonsignificant genes. B. Gene Ontology (GO) and Kyoto Encyclopedia of Genes and Genomes (KEGG) functional enrichment analysis of prognostic

metabolism-related genes. C. Identification of two metabolism-related clusters according to the consensus clustering matrix (k = 2) in the GSE49710 cohort. D. Principal component analysis (PCA) of sample distributions based on metabolism-related clusters. E. Kaplan-Meier curves of overall survival for the two metabolism-related clusters. F, G. Gene set variation analysis (GSVA) of the metabolism-related clusters based on KEGG and hallmark gene sets (indicated by colors).

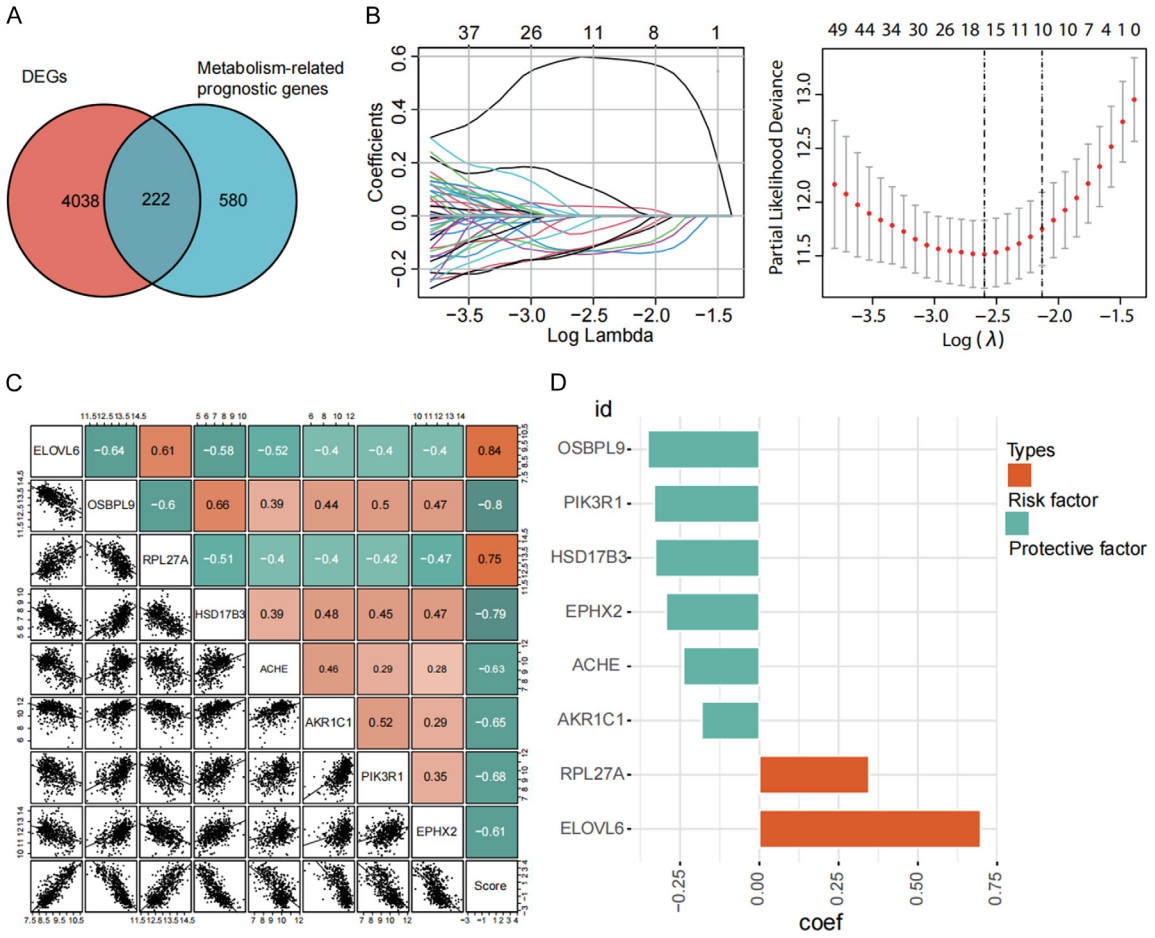

Figure 3. Construction of the metabolism-related risk signature. A. The intersection of prognostic metabolism-related genes and differentially expressed genes (DEGs) between different clusters. B. Least absolute shrinkage and selection operator (LASSO)-Cox regression analysis of the prognostic metabolism-related DEGs. C. Correlation analysis of the eight signature genes and risk scores. D. Coefficient values of the eight signature genes.

potential signature genes (**Figure 3A**). Subsequently, LASSO-penalized Cox regression analysis was applied to the training group to identify eight genes for constructing the metabolism-related risk signature (**Figure 3B**). These signature genes were closely related (**Figure 3C**), and the corresponding regression coefficients are shown in **Figure 3D**.

Samples were categorized into high- and low-risk groups based on the median score. The risk groups were distinctly separated in the training group (**Figure 4A**). Samples in the high-risk group demonstrated shorter survival times (**Figure 4B**, **4C**), and the high-risk group overall exhibited a significantly worse prognosis compared to the low-risk group (**Figure 4D**). The AUC values for the risk signature in predicting 1-year, 3-year, and 5-year overall survival were 0.910, 0.920, and 0.925, respectively (**Figure 4E**).

Internal and external validation of the metabolism-related risk signature

We further validated the risk signature in the internal validation group and two external validation groups, namely the E-MTAB-8248 and

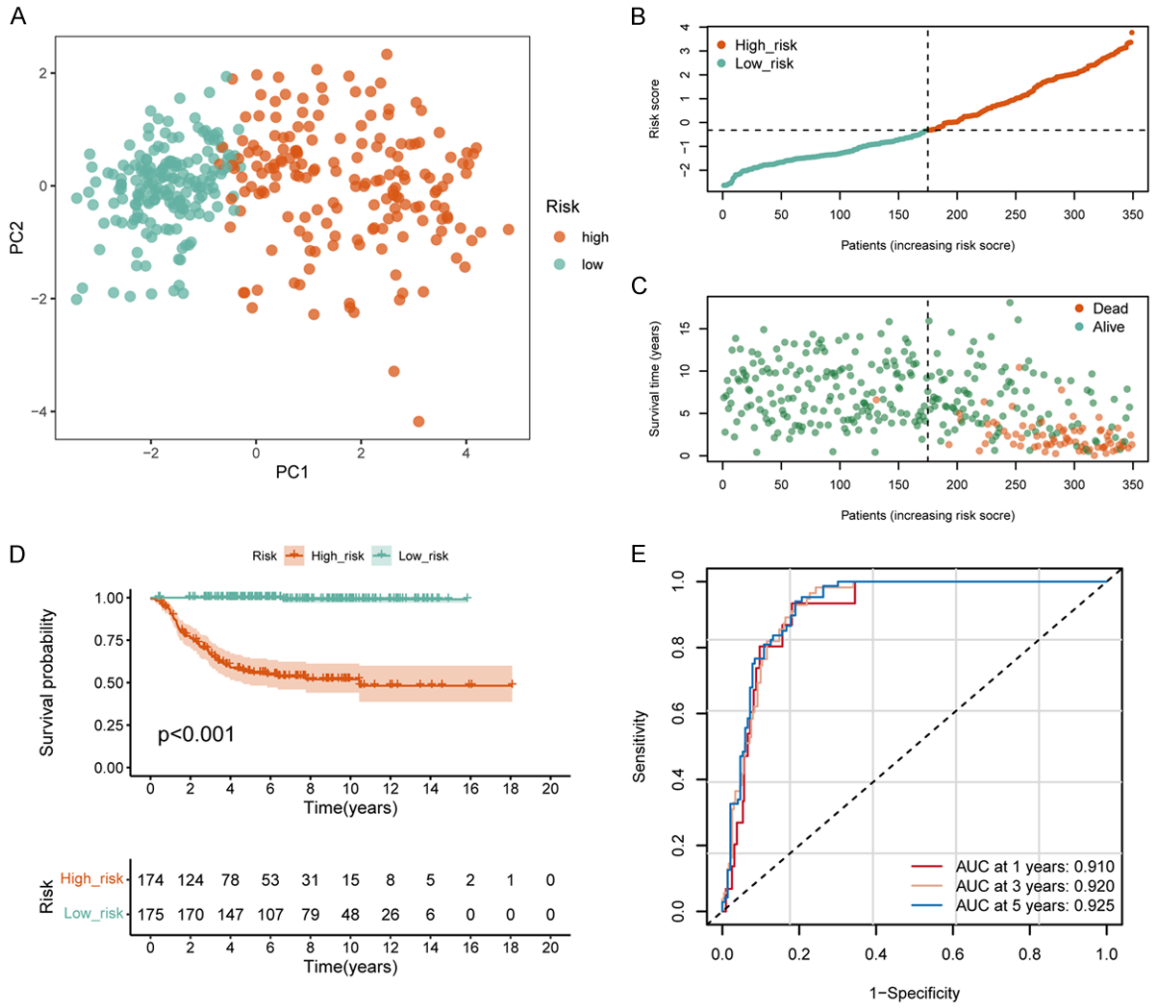

Figure 4. Validation of the metabolism-related signature in the training cohort in GSE49710. (A) PCA plot based on the risk groups. (B, C) The distribution of the risk score (B) and survival time (C) in the training cohort of GSE49710. (D) Kaplan-Meier curves of overall survival (OS) in the training cohort of GSE49710 between the different risk groups. (E) The receiver operating characteristic (ROC) curves of the risk signature for 1-year, 3-year, and 5-year OS prediction in the training cohort of GSE49710.

TARGET cohorts. The risk signature demonstrated significant prognostic value and predictive accuracy in the internal validation group (Figure S2). Notably, it maintained robust prognostic value in the E-MTAB-8248 dataset, accurately predicting prognosis with AUC values exceeding 0.8 throughout the observation period (Figure S3). Similarly, the risk signature showed satisfactory prognostic value and accuracy in the TARGET dataset (Figure S4).

Independent prognosis and GSEA

The risk signature exhibited significant correlations with various clinical characteristics of NB. Samples from patients older than 547 days, with *MYCN* amplification, advanced stage, and disease progression, had significantly higher scores (**Figure 5A**, **5B**). Univariate and multivariate Cox regression analyses established the risk signature as an independent prognostic factor (hazards ratio > 1, P < 0.001, **Figure 5C**, **5D**). Subsequently, we constructed a nomogram to predict 3-year and 5-year overall survival by combining several clinical prognostic factors (**Figure 5E**).

In addition, we explored the differences in biological functions between the high- and low-risk groups. The high-risk group was enriched in cell cycle checkpoint signaling, cell cycle phase transition, and DNA repair (**Figure 6A**), whereas the low-risk group was enriched in immune-related pathways, including regulation of leuko-

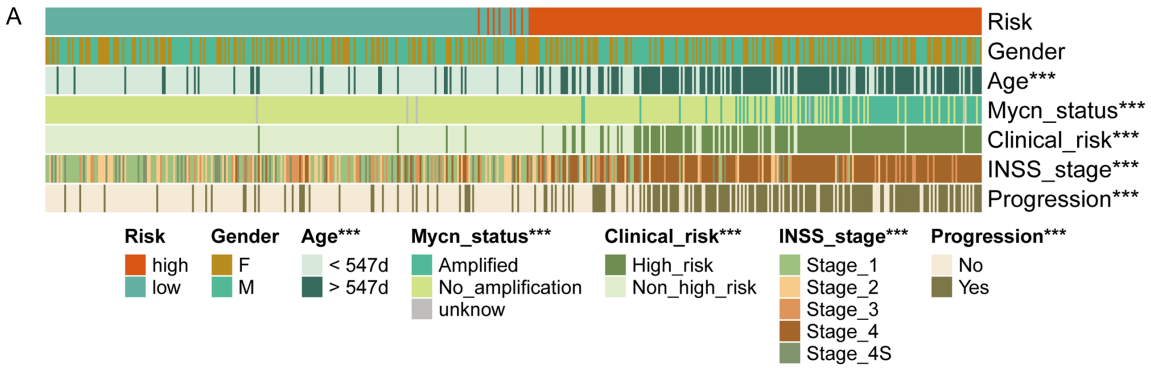
A
Risk
Gender
Age***
Mycn_status***
Clinical_risk***
INSS_stage***
Progression***
Risk
high
low
Gender
F
M
Age***
< 547d
> 547d
Mycn_status***
Amplified
No_amplification
unknow
Clinical_risk***
High_risk
Non_high_risk
INSS_stage***
Stage_1
Stage_2
Stage_3
Stage_4
Stage_4S
Progression***
No
Yes

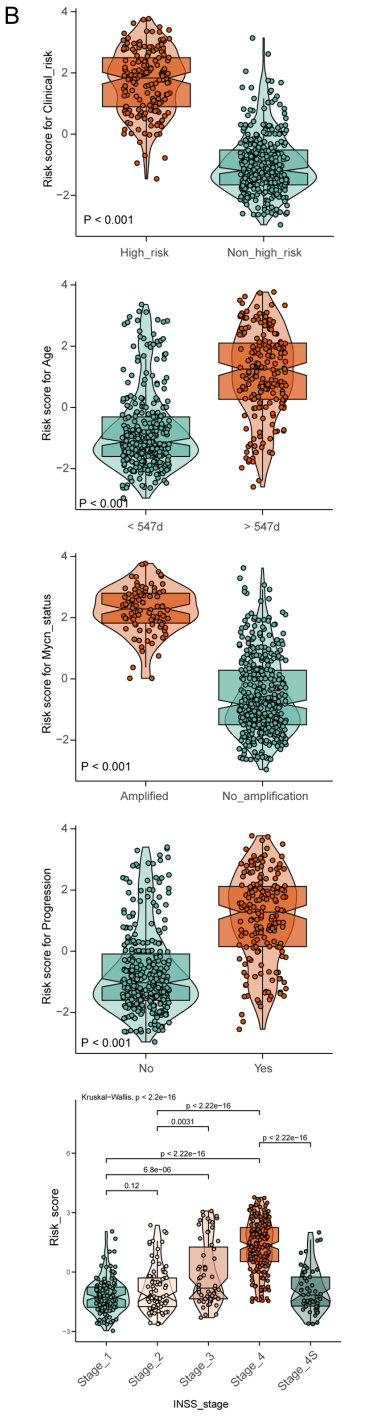
B
Risk score for Clinical_risk
P < 0.001
High_risk
Non_high_risk
Risk score for Age
P < 0.001
< 547d
> 547d
Risk score for Mycn_status
P < 0.001
Amplified
No_amplification
Risk score for Progression
P < 0.001
No
Yes
Kruskal-Wallis, p < 2.2e-16
p < 2.22e-16
0.0031
p < 2.22e-16
p < 2.22e-16
6.8e-06
0.12
Risk_score
Stage_1
Stage_2
Stage_3
Stage_4
Stage_4S
INSS_stage

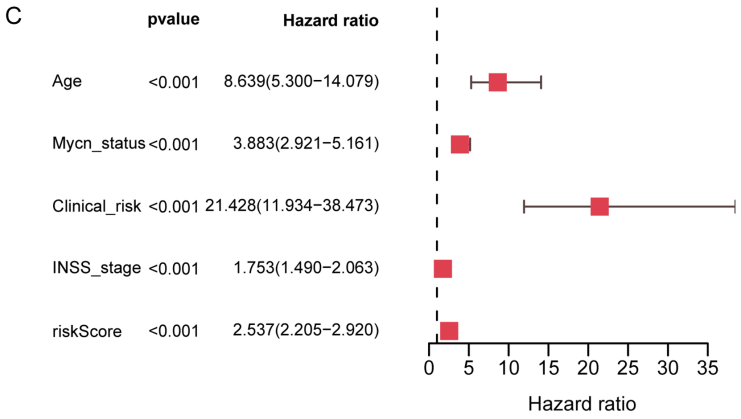
C
pvalue
Hazard ratio
Age <0.001 8.639(5.300−14.079)
Mycn_status <0.001 3.883(2.921−5.161)
Clinical_risk <0.001 21.428(11.934−38.473)
INSS_stage <0.001 1.753(1.490−2.063)
riskScore <0.001 2.537(2.205−2.920)
0 5 10 15 20 25 30 35
Hazard ratio

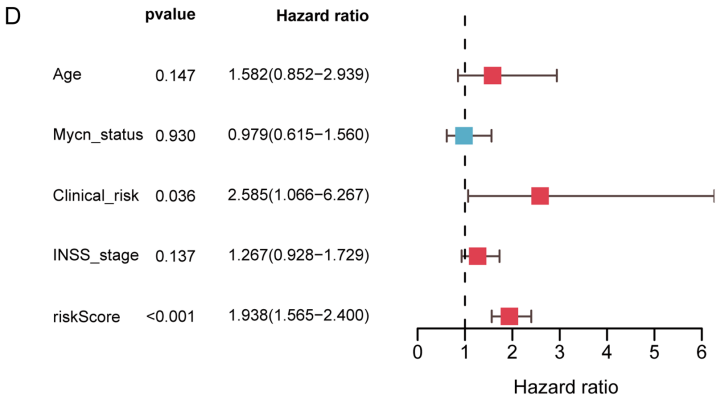
D
pvalue
Hazard ratio
Age 0.147 1.582(0.852−2.939)
Mycn_status 0.930 0.979(0.615−1.560)
Clinical_risk 0.036 2.585(1.066−6.267)
INSS_stage 0.137 1.267(0.928−1.729)
riskScore <0.001 1.938(1.565−2.400)
0 1 2 3 4 5 6
Hazard ratio

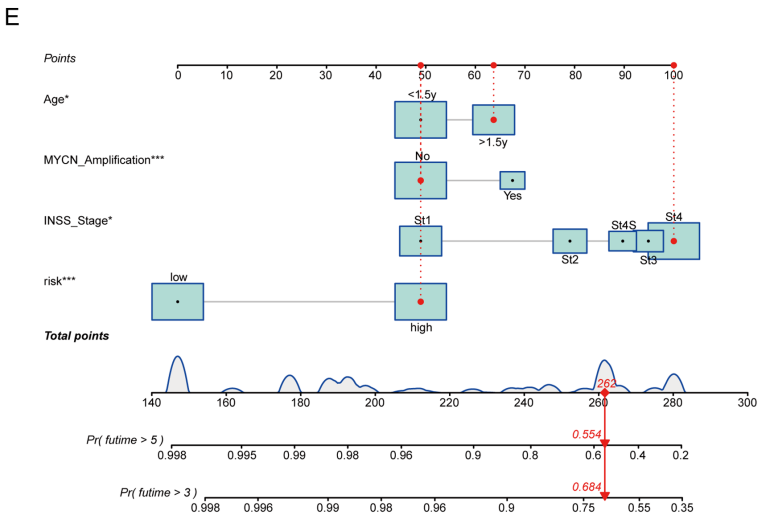
E
Points
0 10 20 30 40 50 60 70 80 90 100
Age*
<1.5y
>1.5y
MYCN_Amplification***
No
Yes
INSS_Stage*
St1
St2
St3
St4S
St4
risk***
low
high
Total points
140 160 180 200 220 240 260 280 300
262
Pr(futime > 5)
0.998 0.995 0.99 0.98 0.96 0.9 0.8 0.6 0.4 0.2
0.554
Pr(futime > 3)
0.998 0.996 0.99 0.98 0.96 0.9 0.75 0.55 0.35
0.684

Figure 5. Correlation analysis between clinical characteristics and the risk signature in the GSE49710 cohort. (A) Heatmap for the relation between clinicopathological characteristics and the risk groups (*: P < 0.05, **: P < 0.01, ***: P < 0.001). (B) Comparison of risk scores between samples with different clinical characteristics, including clinical risk, *MYCN* status, age, progression, and the International Neuroblastoma Staging System (INSS) stage. (C, D) Univariate (C) and (D) multivariate Cox regression analysis of the risk signature in the GSE49710 cohort. (E) The establishment of a nomogram that predicted 3-year and 5-year OS in the GSE49710 cohort.

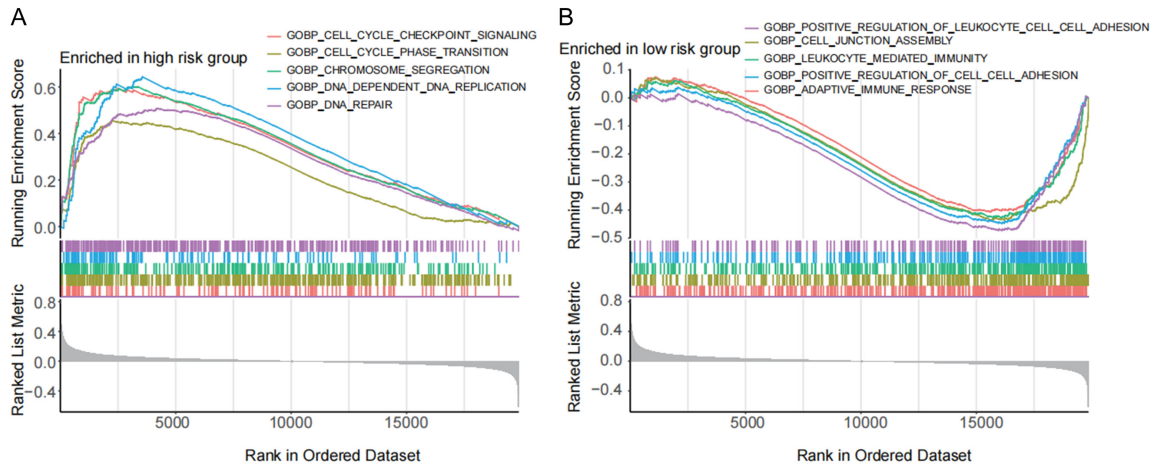

Figure 6. Gene set enrichment analysis (GSEA) of the risk signature. GSEA in the high-risk (A) and low-risk (B) groups.

cyte cell adhesion, leukocyte-mediated immunity, and adaptive immune responses (**Figure 6B**). These findings suggest a potential association of the metabolism-related risk signature with immune infiltration.

Immune infiltration analysis

Considering the enrichment of immune-related pathways in the low-risk, we further analyzed the immune infiltration associated with the risk signature. Notably, most immune cells, such as CD4 and CD8 T cells, showed low infiltration in the high-risk group, indicative of a "cold tumor" phenotype. Conversely, immunosuppressive cells, including stromal cells, were predominantly found in the low-risk group (**Figure 7A**). Consistent with these findings, the stromal and immune scores, determined using the ESTIMATE algorithm, were significantly higher in the low-risk group (**Figure 7B**). Furthermore, several immune-related pathways, like adaptive immune response, T cell activation, and T cell-mediated immunity, were prominently enriched in the low-risk group (**Figure 7C**). Thus, the risk signature identified the high-risk group as exhibiting an immunosuppressive phenotype in NB.

Given the crucial role of immune checkpoints in tumor immunosuppression, we examined their expression in relation to the risk signature. The risk score positively correlated with B7 homolog 3 (CD276) expression, while showing a negative correlation with CD274 (programmed cell death ligand 1 [PD-L1]) and PDCD1LG2 (PD-L2) expression (**Figure 8A**). These immune checkpoints demonstrated varied immunosuppressive mechanisms within the risk signature, suggesting differing immunotherapy strategies for the low- and high-risk groups.

Drug sensitivity

Chemotherapy is an important treatment strategy for NB. To inform clinical treatment, we compared the sensitivity of the two risk groups to various chemotherapeutic agents. Interestingly, the half-maximal inhibitory concentrations of several chemotherapeutic agents, including doxorubicin, cisplatin, etoposide, and vinblastine, were significantly lower in the high-risk group, suggesting that chemotherapy should remain as an applicable treatment for the high-risk group (**Figure 8B**).

The metabolism-related protein ELOVL6 is related to the immune microenvironment and NB prognosis

From the above bioinformatic analysis, we identified *ELOVL6* as an important prognostic mark-

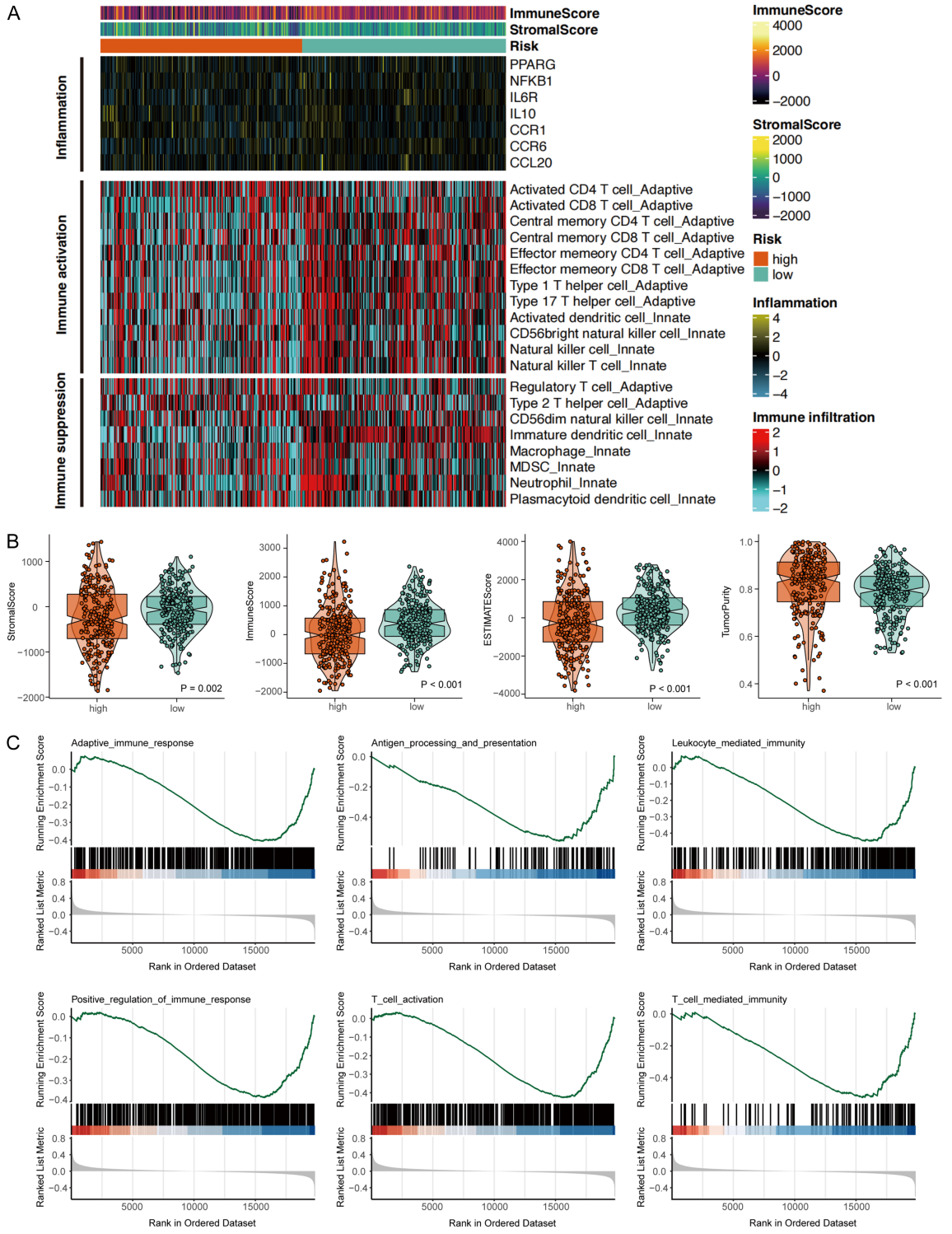

Figure 7. Immune infiltration analysis of the metabolism-related risk signature. A. Heatmap displaying the infiltrating level of immune cells in different risk groups. B. Violin chart comparing differences between the high- and low-risk groups in terms of their stromal score, immune score, ESTIMATE score, and tumor purity. C. GSEA of immune-related pathways in the metabolism-related risk signature (*: P < 0.05, **: P < 0.01, ***: P < 0.001, ****: P < 0.0001).

er in NB, with its expression level correlated with the regulation of the immune microenvironment in NB. To validate the association of ELOVL6 with NB prognosis and immune micro-

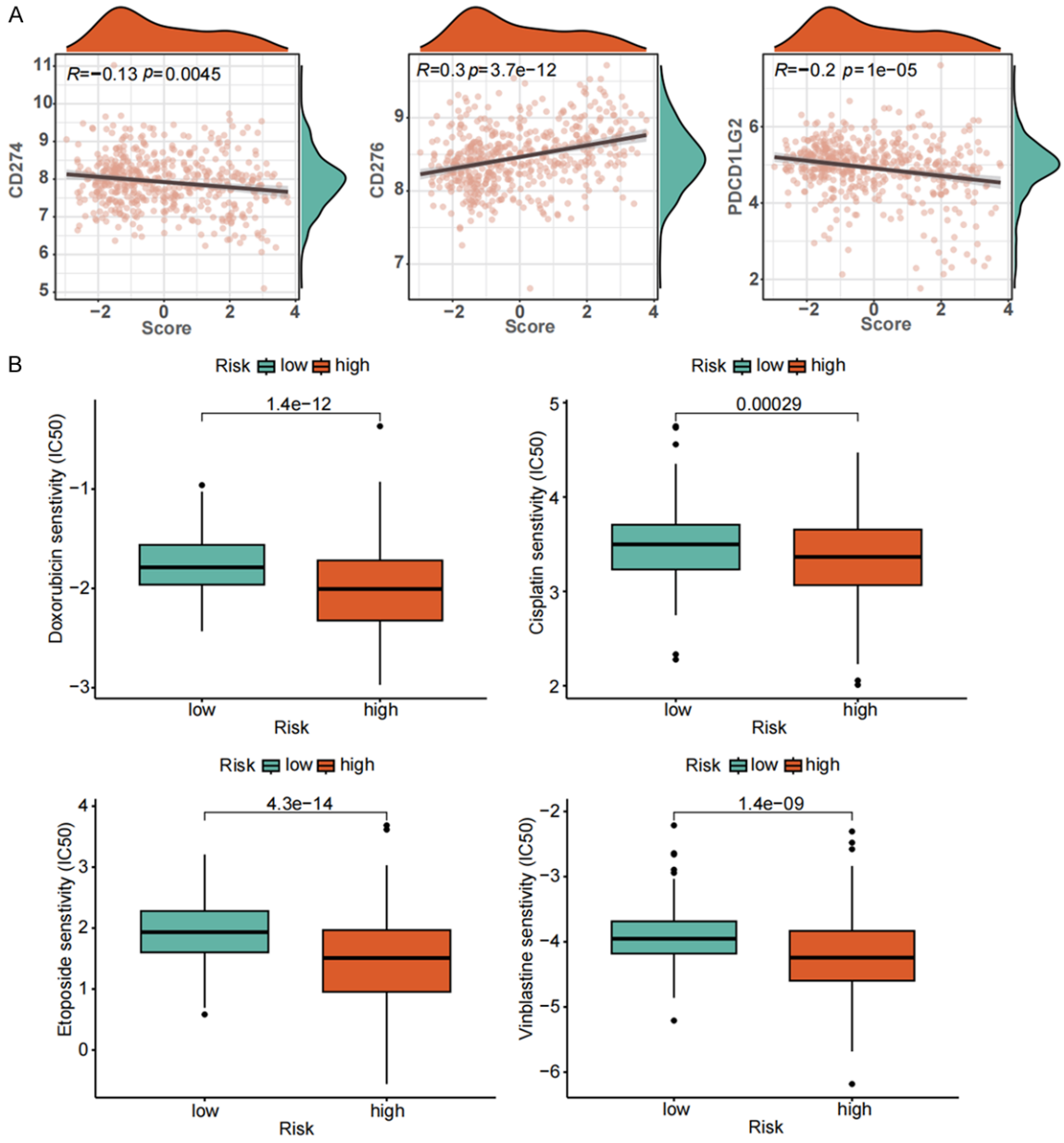

Figure 8. Immune checkpoints and drug sensitivity of the metabolism-related risk signature. A. Correlation between expression of the four immune checkpoints and the metabolism-related risk scores. B. Box plots of estimated half-maximal inhibitory concentrations (IC_{50}) for four chemotherapeutic agents in the high- and low-risk groups.

environment, we analyzed the expression of ELOVL6, CD8, and CD33 (a marker for MDSCs, myeloid-derived suppressor cells) in NB tissues using multicolor immunofluorescence. High CD8 expression correlated with low ELOVL6 expression, while low CD33 expression correlated with high ELOVL6 expression (**Figure 9A**), suggesting that the upregulation of ELOVL6 was associated with an immunosuppressive environment in NB. Using immunohistochemistry, we found that the upregulation of ELOVL6 was associated with both higher grades and worse prognosis according to the International Neuroblastoma Staging System (**Figure 9B**, **9C**).

Expression of ELOVL6 reshapes the immunosuppressive environment in NB

To further explore whether high ELOVL6 expression reshapes the immunosuppressive microenvironment of NB *in vivo*, we engineered

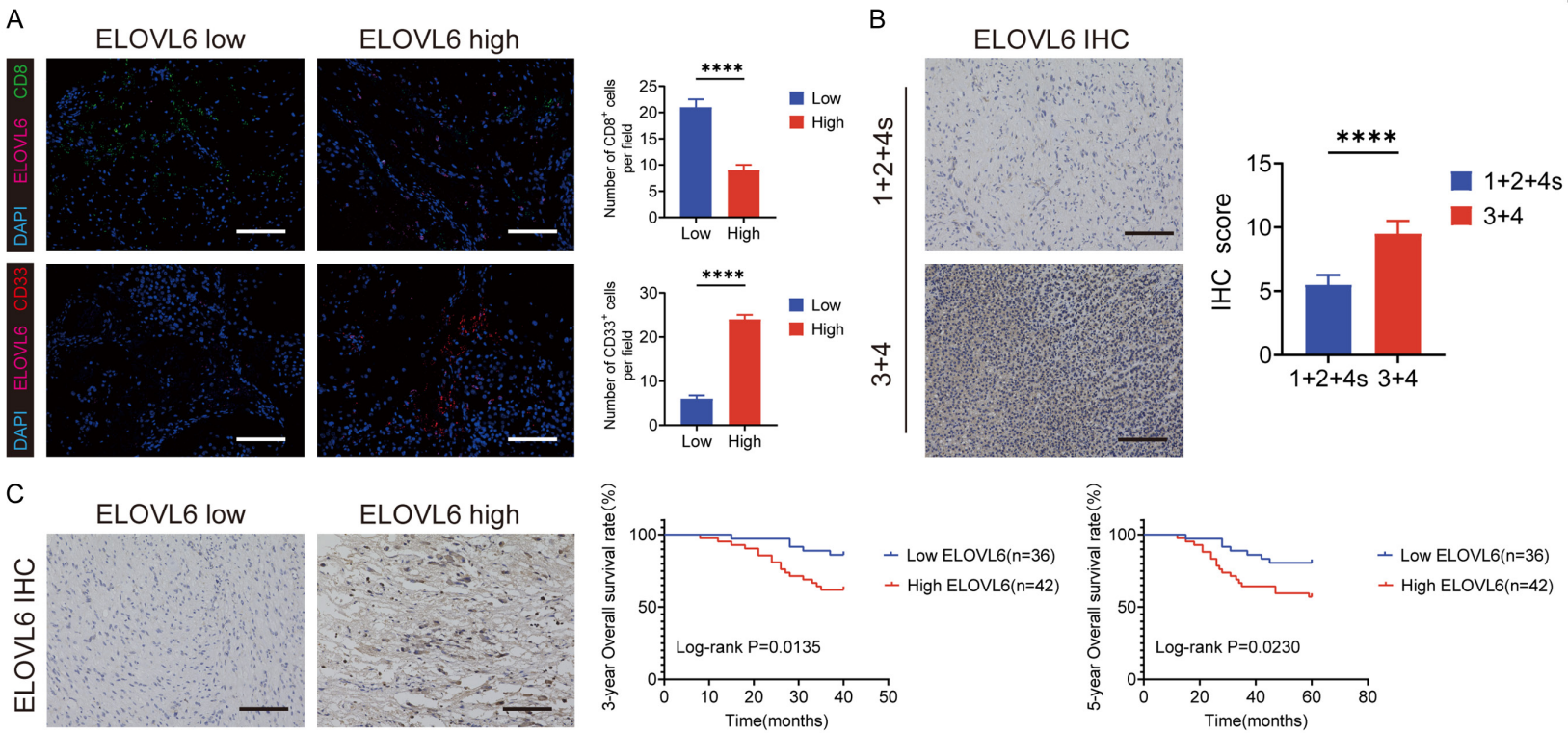

Figure 9. The metabolism-related protein ELOVL6 is related to the immune microenvironment and prognosis of neuroblastoma (NB). A. Representative image of multiplex immunohistochemistry in NB tissue with high or low ELOVL6 expression. Green (CD8), purple (ELOVL6), red (CD33, MDSC), and blue (DAPI). Scale bar: 100 μm. B. The correlation between INSS staging and ELOVL6 expression in NB tissue was analyzed. C. Three-year and five-year overall survival curves were analyzed according to the high or low expression of ELOVL6 in NB patients (n = 78; log-rank test and the *p*-value is shown). Paired Student's t-test was performed for *in vitro* assays and unpaired Student's t-test was conducted for *in vivo* assays. n.s., no significant statistical difference; *, P < 0.05; **, P < 0.01; ***, P < 0.001; ****, P < 0.0001.

the NB cell line 9464D into a stable ELOVL6-Vector/OE cell line and 975A2 into a stable ELOVL6-SC/sh1/sh2 (**Figure 10A**). These cells were implanted into the axillae of C57/BL mice, and tumor growth was recoded every 3 days (Figure 10B). The tumors in the ELOVL6-OE group were significantly larger than those in the ELOVL6-Vector group, while the tumors in the ELOVL6-sh group were significantly smaller than those in the ELOVL6-SC group, indicating more aggressive NB growth with higher ELOVL6 expression (**Figure 10C**, **10D**). Finally, we analyzed the proportions of different immune cells within the tumor tissues of mice from the ELOVL6-Vector/OE/SC/sh groups using flow cytometry. The infiltration of MDSCs (Myeloid-derived suppressor cells) and Treg cells was significantly higher in the ELOVL6-OE group compared with the ELOVL6-Vector group, and lower in the ELOVL6-sh group compared with the ELOVL6-SC group (**Figure 10E**, **10F**). Furthermore, the percentages of CD8+ T cells and cytotoxic factors, such as tumor necrosis factor-α and interferon-γ (IFNγ), were significantly reduced in the ELOVL6-OE group compared with the ELOVL6-Vector group, and higher in the ELOVL6-sh group compared with the ELOVL6-SC group (**Figure 10G-I**). We also examined other relevant immune cells in the tumor immune microenvironment and observed that expression of ELOVL6 elevated exhausted T cells (PD1+ CD8; Tim3+ CD8 cells) (Figure S5A, S5B), further illustrating the properties of ELOVL6 immunosuppression. In addition, ELOVL6 expression did not affect NK cells, M1 (Classical activated macrophages, CD80+ F4/80+), M2 (Alternatively activated macrophages, CD163+ F4/80+), and CD4+ T cells (Figure S5C-F). Overall, these results suggest that high ELOVL6 expression induces an immunosuppressive microenvironment in NB by increasing MDSC and Treg cell infiltration while reducing CD8+ T cell presence.

Discussion

Cellular metabolic reprogramming plays a crucial role in tumorigenesis, significantly affecting gene expression, cell heterogeneity, and the TME in various cancers, including NB, a neuroendocrine tumor that is the leading cause of childhood cancer death [14]. Our study developed a metabolism-related prognostic model for NB, demonstrating a strong correlation between metabolism-related genes and both the immune microenvironment and patient prognosis. Additionally, the lipid metabolism gene ELOVL6 was highlighted, confirming the predictions of our model. This model serves as a reliable reference for analyzing the relationship between the TME and prognosis in NB patients with distinct metabolic profiles.

Lipid and amino acid metabolism have been previously identified as promoters of NB cell growth. Notably, the *MYCN*-activating transcription factor 4 axis, in tandem with epigenetic regulators such as lysine demethylase 4C, enhances the amino acid pool, sustaining *MYCN*-mediated growth in adult NB [15, 16]. Similarly, *MYCN*-enhanced fatty acid oxidation supports NB growth [17]. In this study, we initially categorized patients into two subgroups based on differentially expressed genes enriched in lipid- and amino acid-related metabolism. These subgroups exhibited significant differences in disease-free survival, which corroborates the finding that NB patients with different metabolic backgrounds have different clinical presentations [18]. This finding underscores the necessity of refining the NB clinical prognostic staging system to incorporate lipid and amino acid metabolism.

Single genes often provide limited predictive power; hence, multigene models are frequently employed for prognosis in cancer patients [19]. Several studies have constructed prognostic models using various low-molecular-weight growth factors for cancers like breast, gastric, and osteosarcoma [20-22]. In this study, we screened eight key metabolism-related genes - *ELOVL6*, *OSBPL9*, *RPL27A*, *HSD17B3*, *ACHE*, *AKR1C1*, *PIK3R1*, and *EPHX2* - to construct a prognostic model for NB.

The metabolism-related signature (MRS) has a significant impact on NB prognosis, yet it has been rarely studied, and the genes involved have not been experimentally validated. Our analysis of training and validation sets revealed that MRS influences the clinical characteristics and prognosis of children with NB, in terms of both metabolic immune landscape and immunopharmacological treatment, corroborating the observation that changes in tumor metabolism accompany the progression of NB [23]. Survival analysis, receiver operating characteristic curve analysis, and univariate multifactor

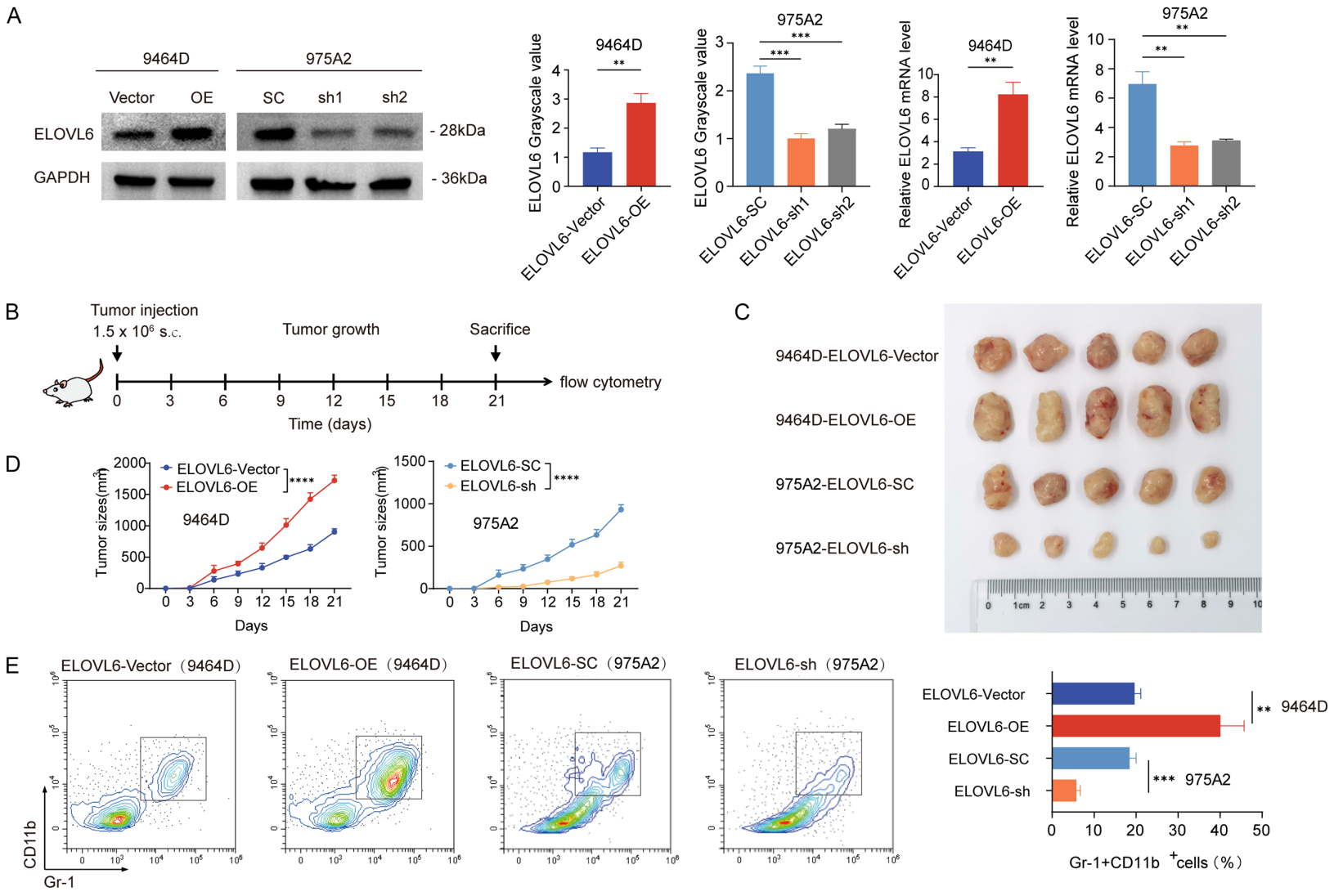
A
9464D
975A2
Vector
OE
SC
sh1
sh2
ELOVL6
GAPDH
- 28kDa
- 36kDa
ELOVL6 Grayscale value
ELOVL6-Vector
ELOVL6-OE
ELOVL6-SC
ELOVL6-sh1
ELOVL6-sh2
Relative ELOVL6 mRNA level
B
Tumor injection
1.5 x 10^6 s.c.
Tumor growth
Sacrifice
flow cytometry
Time (days)
C
9464D-ELOVL6-Vector
9464D-ELOVL6-OE
975A2-ELOVL6-SC
975A2-ELOVL6-sh
D
Tumor sizes(mm^3)
Days
E
CD11b
Gr-1
Gr-1+CD11b +cells (%)

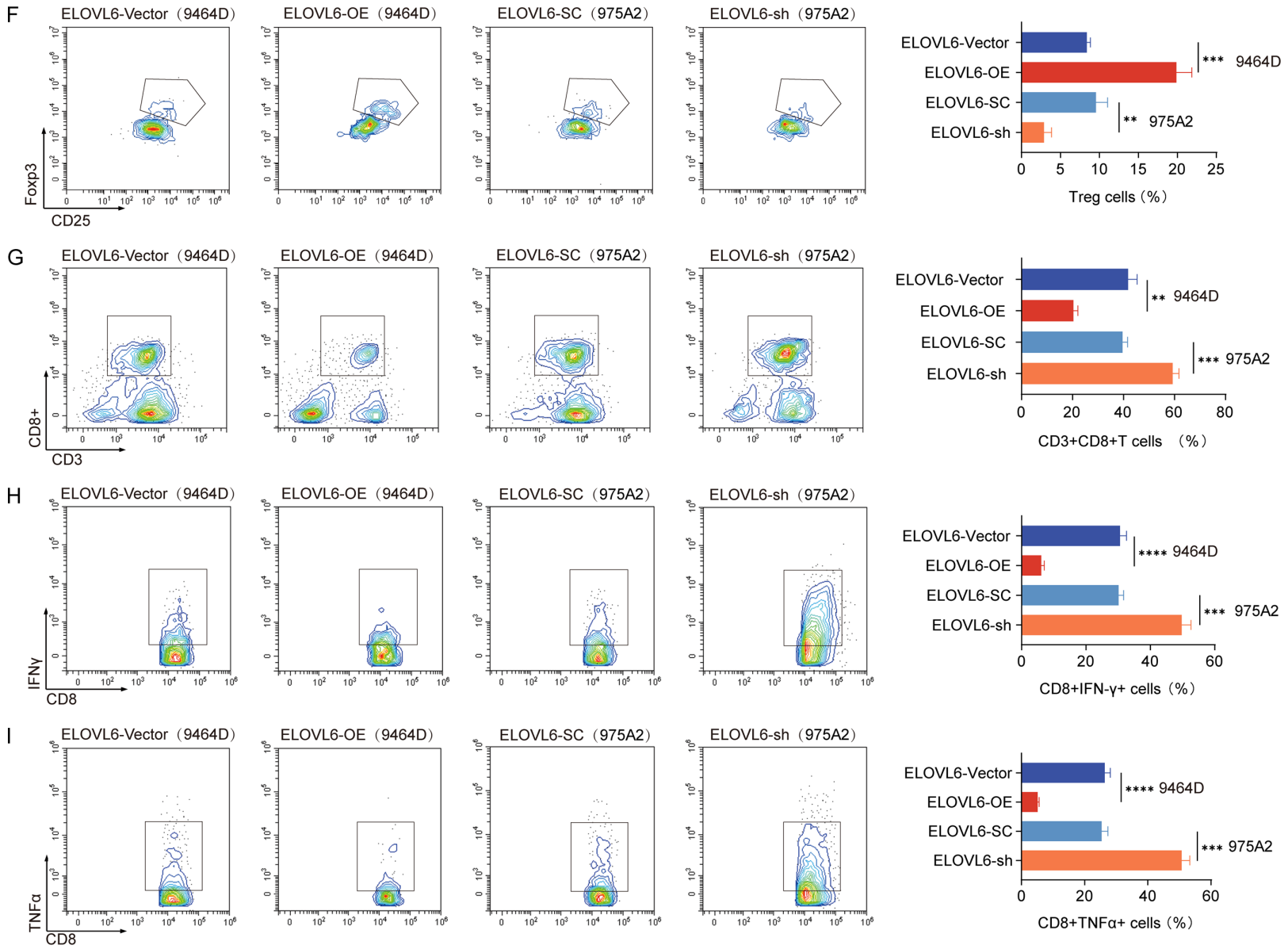

Figure 10. Expression of ELOVL6 reshapes the immunosuppressive environment in NB. (A) Stable expression of ELOVL6 in 9464D cells infected with an ELOVL6 overexpression plasmid, and stable low expression of ELOVL6 in 975A2 cells infected with an ELOVL6 Knockdown plasmid. (B) Vector- or ELOVL6-overexpressing

9464D cells and Scramble- or ELOVL6-sh 975A2 cells were injected into the axilla of C57BL/6 mice (approximately 1.5×10^6 cells per mouse, 5 mice per group). (C, D) The diameters of subcutaneous tumors in mice were measured every 3 days after tumor implantation and a growth curve was plotted. (E-G) Flow cytometric analysis of harvested tumors: Representative dot plots and statistical analysis of the proportions of myeloid-derived suppressor cells (MDSCs) (E), Treg cells (F) and CD3+CD8+ T cells (G). Representative dot plots and statistical analysis of the proportions of tumor-infiltrating CD8+IFNγ+ T cells (H) and CD8+TNFα+ T cells (I). Experiments were independently repeated thrice. Representative data are shown. Data are expressed as the mean ± standard deviation (SD). Paired and unpaired Student's t-tests were performed for *in vitro* and *in vivo* assays, respectively. n.s., no statistically significant difference; *, $P < 0.05$; **, $P < 0.01$; ***, $P < 0.001$; ****, $P < 0.0001$.

Cox regression analysis confirmed that our metabolism-related genes-based model was a reliable and independent prognostic indicator, whose accuracy was considerably higher than other single models.

Typically, NB is considered an immune "cold" tumor, characterized by a lack of reactive T cell infiltration, which contributes to its low response rate to immune checkpoint inhibitors, such as programmed cell death protein 1/PD-L1 inhibitors [24]. We identified eight key methylated DEGs associated with survival, and discovered a strong correlation with the tumor immune microenvironment in NB. Among these, the signature gene *OSBPL9*, which had the highest coefficient value as a protective factor, was downregulated in hepatocellular carcinoma [25]. *PIK3R1* is a tumor suppressor gene [26], and *RPL27A* executes critical functions in the development and metastasis of triple-negative breast cancer [27]. The analysis in this study aligns with these data. *ELOVL6* had the highest coefficient value among risk factors. It was shown to be a poor prognostic predictor in breast and liver cancer [28, 29], but its role in NB had yet to be explored. Through *in vivo* and *in vitro* experiments, we demonstrated that high *ELOVL6* expression in NB led to a significant increase in the infiltration of MDSCs and Treg cells and a significant decrease in the percentage of CD8+ T cells and cytotoxic factors (tumor necrosis factor-α and IFNγ), leading to a worse prognosis. ELOVL6 is a rate-limiting enzyme in the long-chain fatty acid elongation reaction and is involved in lipid metabolism [30]. Previous studies have shown that altered lipid metabolism affects the immunotherapeutic response and can be a promising biomarker for predicting the efficacy of immunotherapy [31]. Therefore, ELOVL6 may contribute to the immunosuppressive in NB by modulating lipid metabolism.

Immune infiltration within the TME is critically associated with tumor ferroptosis, a process that can be induced by interferon-gamma (IFNγ) secreted by CD8+ T cells, key players in antitumor immunity [32]. Ferroptosis in cancer cells can release multiple immunostimulatory signals that further enhance CD8+ T cell infiltration into the tumor [33]. ELOVL6 expression has been reported to inhibit ferroptosis in colon cancer cells [34], suggesting that it may affect patient prognosis in NB via a similar mechanism. In this study, we also found that the high expression of ELOVL6 inhibited ferroptosis in NB cells (Figure S6), which is consistent with studies demonstrating that ferroptosis can be used to kill highly aggressive NB [35].

Current immunotherapy for NB primarily involves anti-disialoganglioside (GD2) monoclonal antibodies. However, some patients experience relapse post anti-GD2 treatment or even turn GD2-negative following relapse. Moreover, GD2 is also expressed in normal tissues. This can lead to neuropathic pain in patients during treatment [36]. Therefore, enhancing immunotherapy efficacy is crucial, not only through the advancement of immunotherapy itself but also via combination with other therapeutic approaches. The immunosuppressive properties of ELOVL6 in NB and its role in inhibiting ferroptosis present a novel therapeutic concept: inhibiting ELOVL6 could promote ferroptosis and immune infiltration in NB, potentially overcoming the limitations and side effects of GD2 monotherapy.

In summary, this study employed the "limma" R package and univariate Cox analysis in combination with LASSO regression analysis to establish metabolism-related gene markers within the NB dataset. An eight-gene signature (*ELOVL6*, *OSBPL9*, *RPL27A*, *HSD17A3*, *ACHE*, *AKR1C1*, *PIK3R1*, *EPHX2*) associated with NB metabolism was identified, effectively predicting disease-free survival. This model was more

comprehensive and accurate, outperforming other single models in predicting tumor prognosis. We selected *ELOVL6* for *in vitro* and *in vivo* validation and found that upregulation promoted the immunosuppressive microenvironment and malignant progression of NB. Taken together, our data demonstrates *ELOVL6* as a potential novel therapeutic target in NB, potentially transforming NB into an immune "hot" tumor, thus addressing the limitations of standalone immunotherapy or ineffective anti-GD2 treatment. We further validated the reliability and detectability of this predictive model, which can inform patient prognosis and guide new immunotherapy combination strategies.

Acknowledgements

This work was supported by Cancer Biobank of Tianjin Medical University Cancer Institute & Hospital; the Natural Science Foundation of Tianjin, China (22JCQNJC00100); the China Postdoctoral Science Foundation (2022M712388 and 2023M732622); the Science & Technology Development Fund of Tianjin Education Commission for Higher Education (2022KJ221); and Tianjin Key Medical Discipline (Specialty) Construction Project (TJYXZDXK-009A).

Written informed consent was obtained from all patients.

Disclosure of conflict of interest

None.

Address correspondence to: Dr. Chao Wu, Yongjie Xie and Weishuai Liu, Tianjin Medical University Cancer Institute and Hospital, National Clinical Research Center for Cancer, Tianjin's Clinical Research Center for Cancer, Key Laboratory of Cancer Immunology and Biotherapy, Huanhu West Road, Hexi District, Tianjin, China. Tel: +86-19902099629; E-mail: wuchaozhicheng@126.com (CW); 2335940013@qq.com (YJX); liuweishuai@126.com (WSL)

References

[1] Matthay KK, Maris JM, Schleiermacher G, Nakagawara A, Mackall CL, Diller L and Weiss WA. Neuroblastoma. Nat Rev Dis Primers 2016; 2: 16078.

[2] Qiu B and Matthay KK. Advancing therapy for neuroblastoma. Nat Rev Clin Oncol 2022; 19: 515-533.

[3] Zafar A, Wang W, Liu G, Wang X, Xian W, McKeon F, Foster J, Zhou J and Zhang R. Molecular targeting therapies for neuroblastoma: progress and challenges. Med Res Rev 2021; 41: 961-1021.

[4] Faubert B, Solmonson A and DeBerardinis RJ. Metabolic reprogramming and cancer progression. Science 2020; 368: eaaw5473.

[5] Wang Y, Xia Y and Lu Z. Metabolic features of cancer cells. Cancer Commun (Lond) 2018; 38: 65.

[6] Fischer K, Hoffmann P, Voelkl S, Meidenbauer N, Ammer J, Edinger M, Gottfried E, Schwarz S, Rothe G, Hoves S, Renner K, Timischl B, Mackensen A, Kunz-Schughart L, Andreesen R, Krause SW and Kreutz M. Inhibitory effect of tumor cell-derived lactic acid on human T cells. Blood 2007; 109: 3812-3819.

[7] Goetze K, Walenta S, Ksiazkiewicz M, Kunz-Schughart LA and Mueller-Klieser W. Lactate enhances motility of tumor cells and inhibits monocyte migration and cytokine release. Int J Oncol 2011; 39: 453-463.

[8] Currie E, Schulze A, Zechner R, Walther TC and Farese RV Jr. Cellular fatty acid metabolism and cancer. Cell Metab 2013; 18: 153-161.

[9] Zhang W, Yu Y, Hertwig F, Thierry-Mieg J, Zhang W, Thierry-Mieg D, Wang J, Furlanello C, Devanarayan V, Cheng J, Deng Y, Hero B, Hong H, Jia M, Li L, Lin SM, Nikolsky Y, Oberthuer A, Qing T, Su Z, Volland R, Wang C, Wang MD, Ai J, Albanese D, Asgharzadeh S, Avigad S, Bao W, Bessarabova M, Brilliant MH, Brors B, Chierici M, Chu TM, Zhang J, Grundy RG, He MM, Hebbring S, Kaufman HL, Lababidi S, Lancashire LJ, Li Y, Lu XX, Luo H, Ma X, Ning B, Noguera R, Peifer M, Phan JH, Roels F, Rosswog C, Shao S, Shen J, Theissen J, Tonini GP, Vandesompele J, Wu PY, Xiao W, Xu J, Xu W, Xuan J, Yang Y, Ye Z, Dong Z, Zhang KK, Yin Y, Zhao C, Zheng Y, Wolfinger RD, Shi T, Malkas LH, Berthold F, Wang J, Tong W, Shi L, Peng Z and Fischer M. Comparison of RNA-seq and microarray-based models for clinical endpoint prediction. Genome Biol 2015; 16: 133.

[10] Wilkerson MD and Hayes DN. ConsensusClusterPlus: a class discovery tool with confidence assessments and item tracking. Bioinformatics 2010; 26: 1572-1573.

[11] Liu Z, Guo Y, Yang X, Chen C, Fan D, Wu X, Si C, Xu Y, Shao B, Chen Z, Dang Q, Cui W, Han X, Ji Z and Sun Z. Immune landscape refines the classification of colorectal cancer with heterogeneous prognosis, tumor microenvironment

and distinct sensitivity to frontline therapies. Front Cell Dev Biol 2022; 9: 784199.
[12] Charoentong P, Finotello F, Angelova M, Mayer C, Efremova M, Rieder D, Hackl H and Trajanoski Z. Pan-cancer immunogenomic analyses reveal genotype-immunophenotype relationships and predictors of response to checkpoint blockade. Cell Rep 2017; 18: 248-262.
[13] Yoshihara K, Shahmoradgoli M, Martinez E, Vegesna R, Kim H, Torres-Garcia W, Trevino V, Shen H, Laird PW, Levine DA, Carter SL, Getz G, Stemke-Hale K, Mills GB and Verhaak RG. Inferring tumour purity and stromal and immune cell admixture from expression data. Nat Commun 2013; 4: 2612.
[14] Bansal M, Gupta A and Ding HF. MYCN and metabolic reprogramming in neuroblastoma. Cancers (Basel) 2022; 14: 4113.
[15] Xia Y, Ye B, Ding J, Yu Y, Alptekin A, Thangaraju M, Prasad PD, Ding ZC, Park EJ, Choi JH, Gao B, Fiehn O, Yan C, Dong Z, Zha Y and Ding HF. Metabolic reprogramming by MYCN confers dependence on the serine-glycine-one-carbon biosynthetic pathway. Cancer Res 2019; 79: 3837-3850.
[16] Liu M, Xia Y, Ding J, Ye B, Zhao E, Choi JH, Alptekin A, Yan C, Dong Z, Huang S, Yang L, Cui H, Zha Y and Ding HF. Transcriptional profiling reveals a common metabolic program in high-risk human neuroblastoma and mouse neuroblastoma sphere-forming cells. Cell Rep 2016; 17: 609-623.
[17] Oliynyk G, Ruiz-Perez MV, Sainero-Alcolado L, Dzieran J, Zirath H, Gallart-Ayala H, Wheelock CE, Johansson HJ, Nilsson R, Lehtio J and Arsenian-Henriksson M. MYCN-enhanced oxidative and glycolytic metabolism reveals vulnerabilities for targeting neuroblastoma. iScience 2019; 21: 188-204.
[18] Ponzoni M, Bachetti T, Corrias MV, Brignole C, Pastorino F, Calarco E, Bensa V, Giusto E, Ceccherini I and Perri P. Recent advances in the developmental origin of neuroblastoma: an overview. J Exp Clin Cancer Res 2022; 41: 92.
[19] Balachandran VP, Gonen M, Smith JJ and DeMatteo RP. Nomograms in oncology: more than meets the eye. Lancet Oncol 2015; 16: e173-180.
[20] Ye Z, Zou S, Niu Z, Xu Z and Hu Y. A novel risk model based on lipid metabolism-associated genes predicts prognosis and indicates immune microenvironment in breast cancer. Front Cell Dev Biol 2021; 9: 691676.
[21] Wei XL, Luo TQ, Li JN, Xue ZC, Wang Y, Zhang Y, Chen YB and Peng C. Development and validation of a prognostic classifier based on lipid metabolism-related genes in gastric cancer. Front Mol Biosci 2021; 8: 691143.
[22] Su C, Wang X, Zhou J, Zhao J, Zhou F, Zhao G, Xu X, Zou X, Zhu B and Jia Q. Titin mutation in circulatory tumor DNA is associated with efficacy to immune checkpoint blockade in advanced non-small cell lung cancer. Transl Lung Cancer Res 2021; 10: 1256-1265.
[23] Sakowicz-Burkiewicz M, Pawelczyk T and Zysk M. Role of energy metabolism in the progression of neuroblastoma. Int J Mol Sci 2021; 22: 11421.
[24] Casey DL and Cheung NV. Immunotherapy of pediatric solid tumors: treatments at a crossroads, with an emphasis on antibodies. Cancer Immunol Res 2020; 8: 161-166.
[25] Tian K, Ying Y, Huang J, Wu H, Wei C, Li L, Chen L and Wu L. The expression, immune infiltration, prognosis, and experimental validation of OSBPL family genes in liver cancer. BMC Cancer 2023; 23: 244.
[26] Liu Y, Wang D, Li Z, Li X, Jin M, Jia N, Cui X, Hu G, Tang T and Yu Q. Pan-cancer analysis on the role of PIK3R1 and PIK3R2 in human tumors. Sci Rep 2022; 12: 5924.
[27] Zhao W, Li X, Nian W, Wang J, Wang X, Sun L, Zhu Y and Tong Z. Ribosome proteins represented by RPL27A mark the development and metastasis of triple-negative breast cancer in mouse and human. Front Cell Dev Biol 2021; 9: 716730.
[28] Su YC, Feng YH, Wu HT, Huang YS, Tung CL, Wu P, Chang CJ, Shiau AL and Wu CL. Elovl6 is a negative clinical predictor for liver cancer and knockdown of Elovl6 reduces murine liver cancer progression. Sci Rep 2018; 8: 6586.
[29] Feng YH, Chen WY, Kuo YH, Tung CL, Tsao CJ, Shiau AL and Wu CL. Elovl6 is a poor prognostic predictor in breast cancer. Oncol Lett 2016; 12: 207-212.
[30] Matsuzaka T and Shimano H. Role of fatty acid elongase Elovl6 in the regulation of fatty acid quality and lifestyle-related diseases. Yakugaku Zasshi 2022; 142: 473-476.
[31] Ma Y, Zhang S, Jin Z and Shi M. Lipid-mediated regulation of the cancer-immune crosstalk. Pharmacol Res 2020; 161: 105131.
[32] Wang W, Green M, Choi JE, Gijon M, Kennedy PD, Johnson JK, Liao P, Lang X, Kryczek I, Sell A, Xia H, Zhou J, Li G, Li J, Li W, Wei S, Vatan L, Zhang H, Szeliga W, Gu W, Liu R, Lawrence TS, Lamb C, Tanno Y, Cieslik M, Stone E, Georgiou G, Chan TA, Chinnaiyan A and Zou W. CD8(+) T cells regulate tumour ferroptosis during cancer immunotherapy. Nature 2019; 569: 270-274.
[33] Ma X, Xiao L, Liu L, Ye L, Su P, Bi E, Wang Q, Yang M, Qian J and Yi Q. CD36-mediated ferroptosis dampens intratumoral CD8(+) T cell effector function and impairs their antitumor ability. Cell Metab 2021; 33: 1001-1012, e1005.

[34] Tian X, Li S and Ge G. Apatinib promotes ferroptosis in colorectal cancer cells by targeting ELOVL6/ACSL4 signaling. Cancer Manag Res 2021; 13: 1333-1342.
[35] Lu Y, Yang Q, Su Y, Ji Y, Li G, Yang X, Xu L, Lu Z, Dong J, Wu Y, Bei JX, Pan C, Gu X and Li B. MYCN mediates TFRC-dependent ferroptosis and reveals vulnerabilities in neuroblastoma. Cell Death Dis 2021; 12: 511.
[36] Mastrangelo S, Rivetti S, Triarico S, Romano A, Attina G, Maurizi P and Ruggiero A. Mechanisms, characteristics, and treatment of neuropathic pain and peripheral neuropathy associated with dinutuximab in neuroblastoma patients. Int J Mol Sci 2021; 22: 12648.

Table S2. Patient clinical features

Characteristic	Patient number (percentage)
Total	78
Age (months)	
< 18	23 (29.5%)
≥ 18	55 (70.5%)
Sex	
Male	34 (43.6%)
Female	44 (56.4%)
INSS stage	
1	16 (20.5%)
2	5 (6.4%)
3	17 (21.8%)
4	38 (48.7%)
4s	2 (2.6%)
MYCN status	
Amplification	18 (23.1%)
Not amplification	60 (76.9%)
Risk group	
LR	19 (24.4%)
IR	20 (25.6%)
HR	39 (50.0%)
Bone marrow metastasis	
Yes	31 (39.7%)
No	47 (60.3%)
LDH (U/L)	
≤295	12 (15.4%)
295-500	21 (26.9%)
500-1500	32 (41.0%)
> 1500	11 (14.1%)
None	2 (2.6%)
NSE (ng/l)	
≤25	16 (20.5%)
25-100	25 (32.1%)
> 100	37 (47.4%)
VMA (mg/24 h urine)	
≤13.6	5 (6.4%)
> 13.6	50 (64.1%)
None	23 (29.5%)
Follow-up	
Alive	53 (67.9%)
Dead	25 (32.1%)

Table S3. The primary antibodies utilized for western blot analysis, immunochemistry, flow cytometry, and muticolor-immunofluorescence

Antibody	Company	Catalog Number	Dilution
ELOVL6	Abcam	ab69857	1-2 ug/ml
ACSL4	ABclonal	A20414	1:10000
GPx4	Cell Signaling Technology	59735	1:1000
FTH1	Cell Signaling Technology	4393	1:1000
GAPDH	Cell Signaling Technology	5174	1:1000
ELOVL6	Abcam	ab69857	5 ug/ml
APC/Fire 750 anti-mouse CD45	BioLegend	103154	1:100
FITC anti-mouse CD8a	BioLegend	100706	1:100
APC-anti-mouse-CD3	BioLegend	100236	1:100
APC-anti-mouse/human CD11b	BioLegend	101212	1:100
eFluor™ 450 anti-mouse Gr-1	Invitrogen	48-5931-82	1:100
Brilliant Violet 605™anti-mouse TNF-α	BioLegend	506329	1:100
PE-anti-mouse-IFNγ	Invitrogen	12-7311-82	1:100
BUV395 CD25	BD	564022	1:100
PerCP-eFluor710 FOXP3	THERMO	46-5773-82	1:100
SuperBright 600 PD1	eBioscience	63-9981-82	1:100
PE/dazzle 594 anti-mouse CD366 (Tim-3)	BioLegend	134014	1:100
Brilliant Violet 785™ anti-mouse NK-1.1	BioLegend	108749	1:100
Brilliant Violet 785™ anti-mouse F4/80	BioLegend	123141	1:100
Brilliant Violet 421™ anti-mouse CD80	BioLegend	104726	1:100
SuperBright600 CD163	THERMO	63-1631-82	1:100
Brilliant Violet 421™ anti-mouse CD4	BioLegend	100544	1:100
ELOVL6	Abcam	ab69857	1 ug/ml
CD8	ZSGB-BIO	ZA-0508	/
CD33	ZSGB-BIO	ZM-0045	/
DAPI	SouthernBiotech	0100-20	/

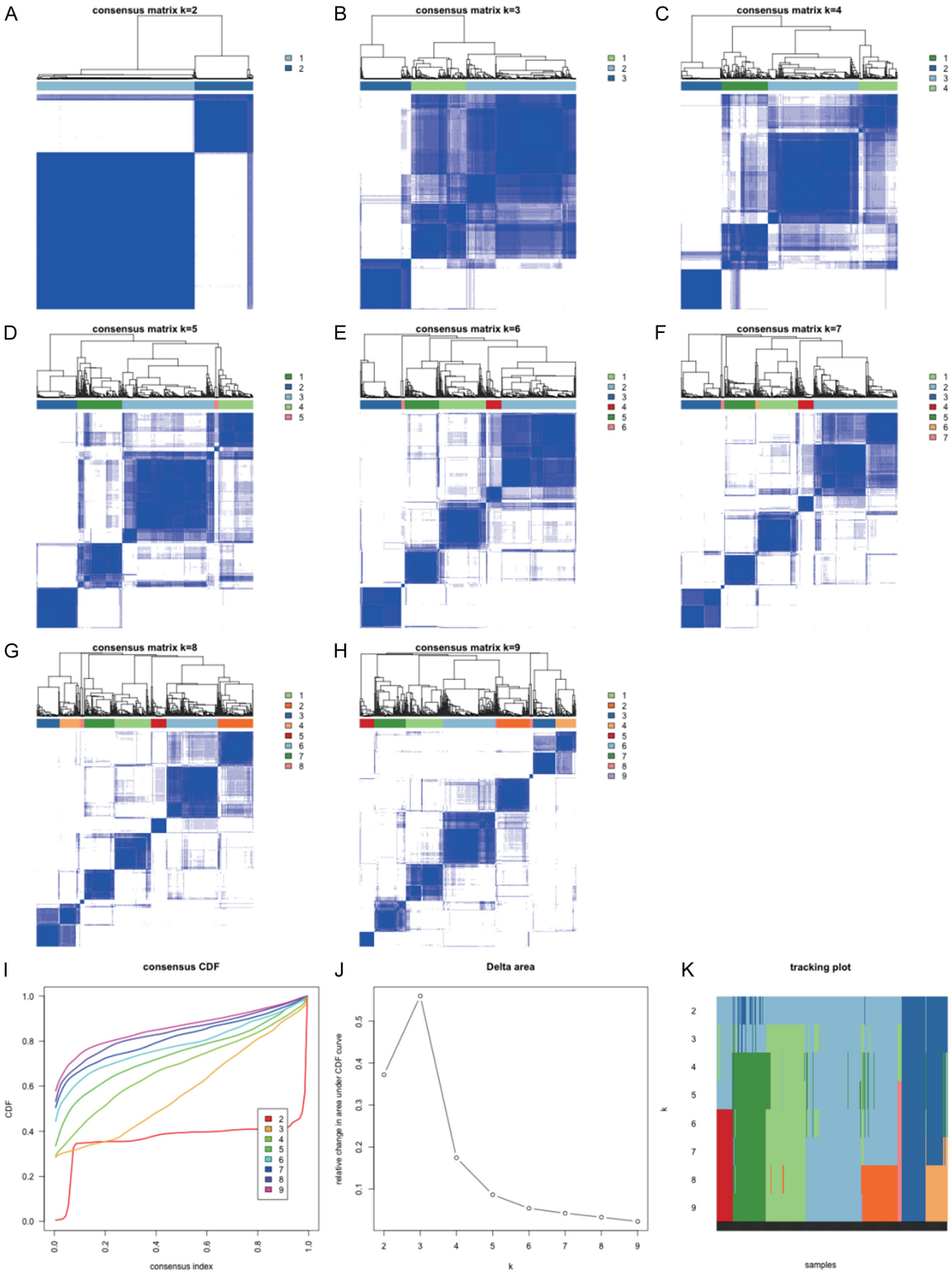

Figure S1. Consensus clustering analysis based on prognostic metabolism-related genes in the GSE49710 dataset. A-H. Consensus score matrix of samples when k = 2-9. I. Cumulative distribution function (CDF) of the consensus matrix for each k (indicated by colors). J. Tracking plot for each k. K. Relative alterations in the area under CDF curves.

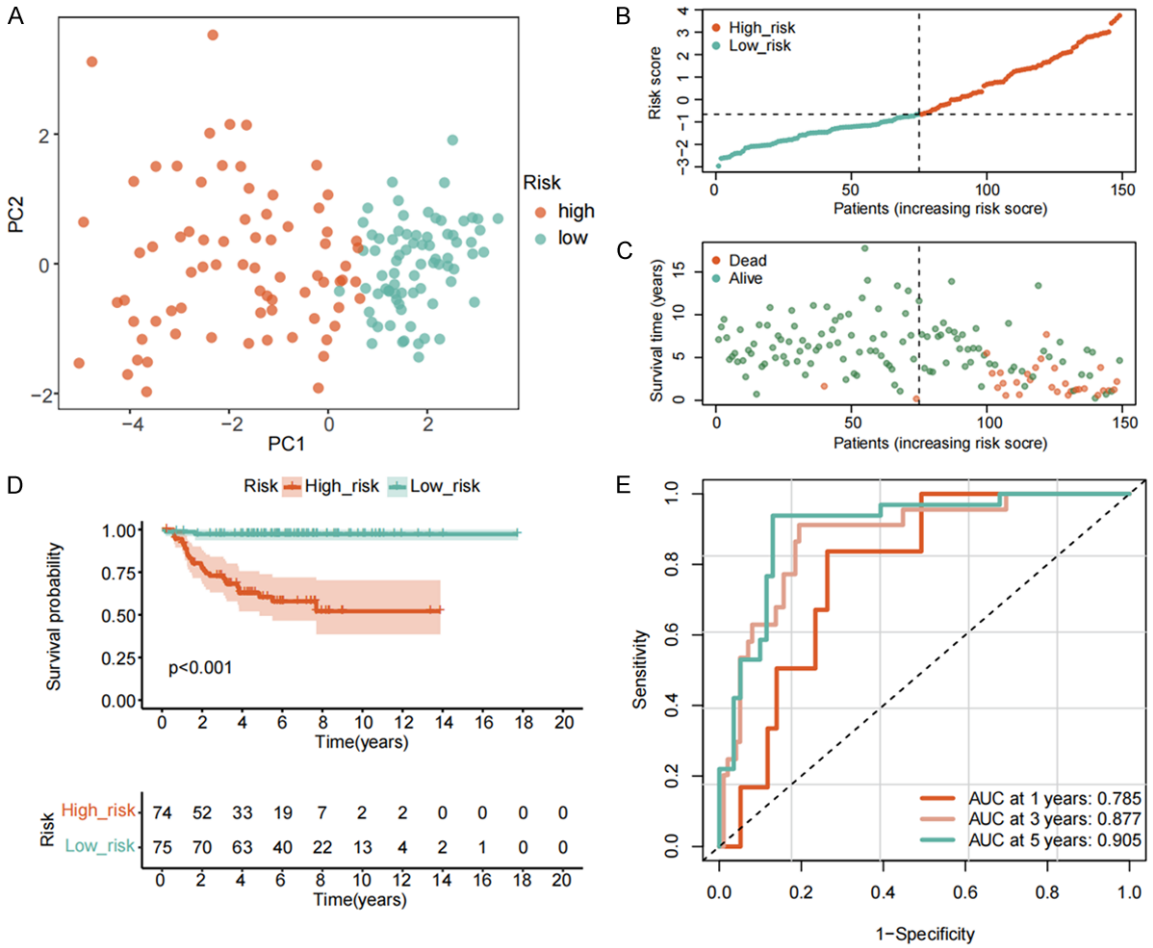

Figure S2. Validation of the metabolism-related signature in the testing cohort in the GSE49710 dataset. (A) Principal component analysis (PCA) plot based on the risk groups. (B, C) The distribution of the risk score (B) and survival time (C) in the testing cohort in the GSE49710 dataset. (D) Kaplan-Meier curves of overall survival (OS) in the testing cohort in the GSE49710 dataset. (E) Receiver operating characteristic (ROC) curves of the risk signature for 1-year, 3-year, and 5-year OS prediction in the testing cohort in the GSE49710 dataset.

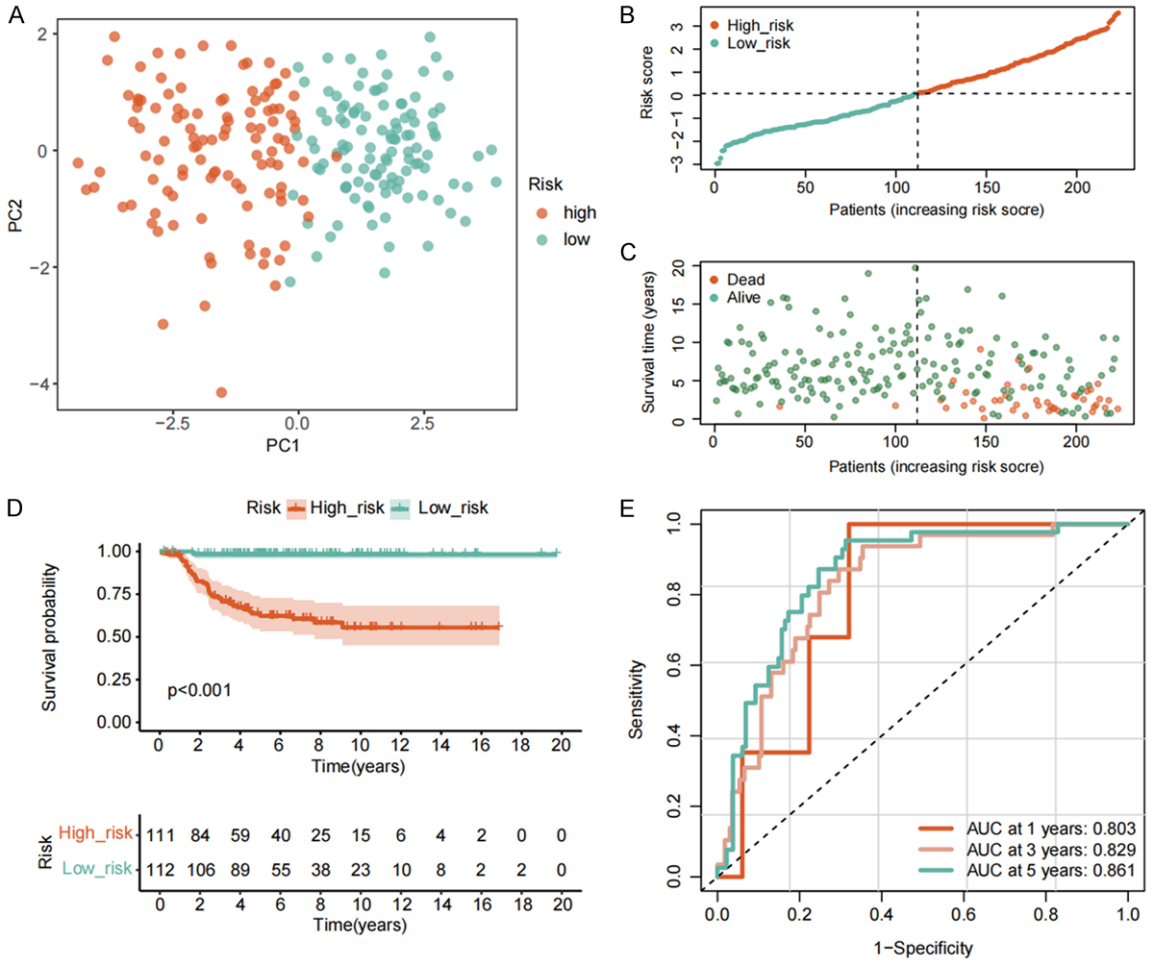

Figure S3. Validation of the metabolism-related signature in the E-MTAB-8248 dataset. (A) PCA plot based on the risk groups. (B, C) The distribution of the risk score (B) and survival time (C) in the testing cohort in the E-MTAB-8248 dataset. (D) Kaplan-Meier curves of OS in the testing cohort in the E-MTAB-8248 dataset. (E) ROC curves of the risk signature for 1-year, 3-year, and 5-year OS prediction in the testing cohort in the E-MTAB-8248 dataset.

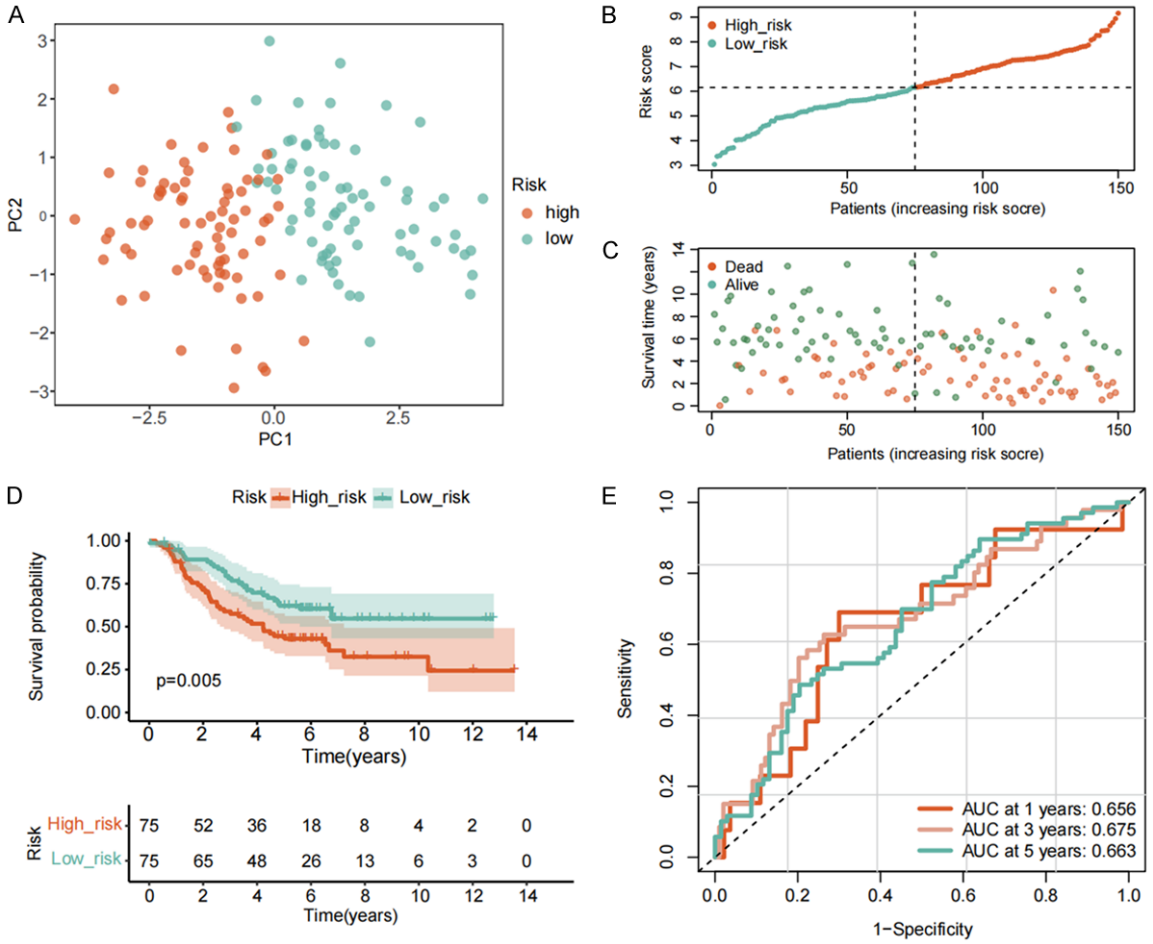

Figure S4. Validation of the metabolism-related signature in the TARGET cohort. (A) PCA plot based on the risk groups. (B, C) The distribution of the risk score (B) and survival time (C) in the TARGET cohort. (D) Kaplan-Meier curves of OS in the testing cohort in the TARGET cohort. (E) ROC curves of the risk signature for 1-year, 3-year, and 5-year OS prediction in the testing cohort in the TARGET cohort.

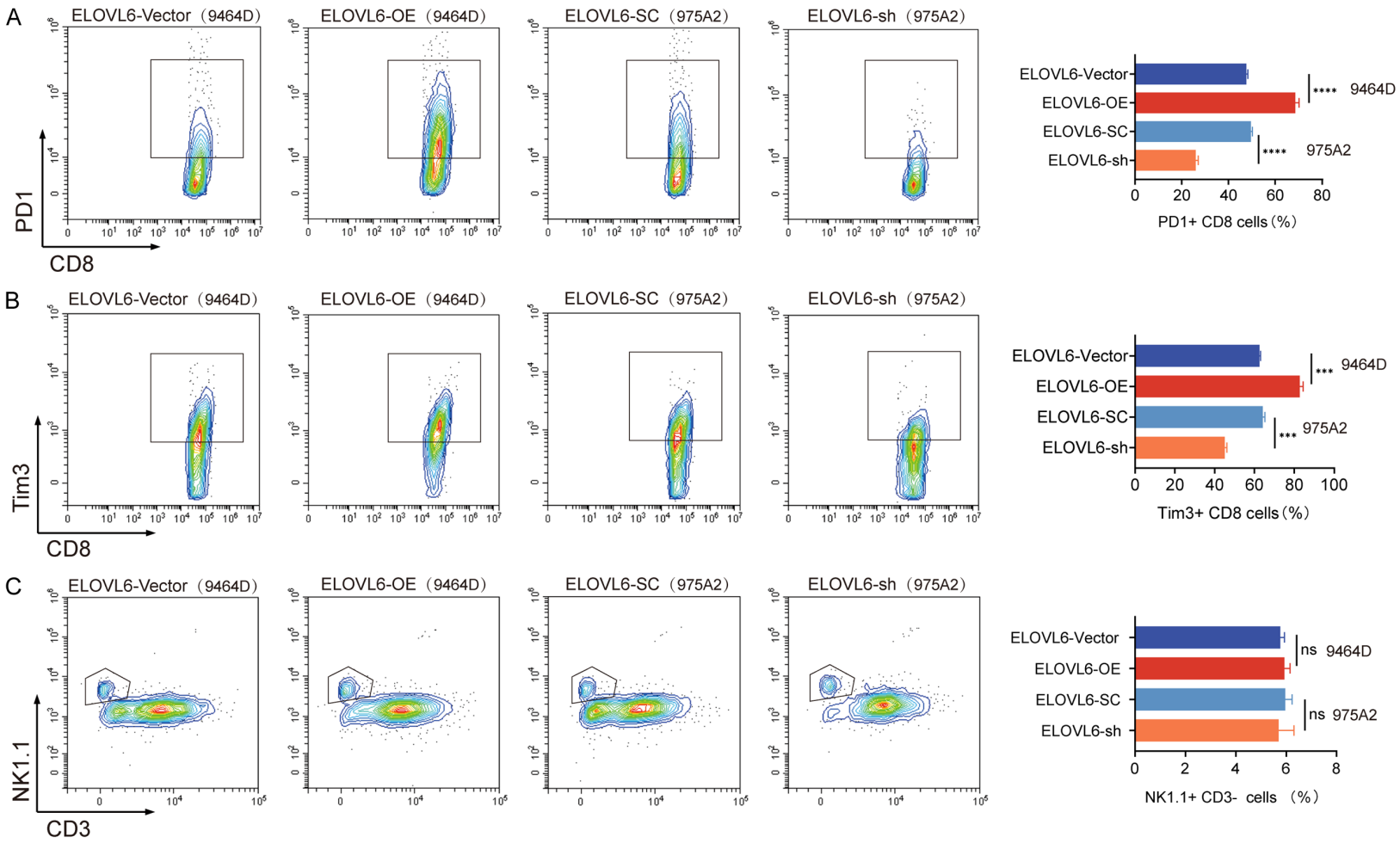
A
ELOVL6-Vector（9464D）
ELOVL6-OE（9464D）
ELOVL6-SC（975A2）
ELOVL6-sh（975A2）
PD1
CD8
ELOVL6-Vector
ELOVL6-OE
ELOVL6-SC
ELOVL6-sh
****
9464D
****
975A2
0 20 40 60 80
PD1+ CD8 cells（%）
B
ELOVL6-Vector（9464D）
ELOVL6-OE（9464D）
ELOVL6-SC（975A2）
ELOVL6-sh（975A2）
Tim3
CD8
ELOVL6-Vector
ELOVL6-OE
ELOVL6-SC
ELOVL6-sh
***
9464D
***
975A2
0 20 40 60 80 100
Tim3+ CD8 cells（%）
C
ELOVL6-Vector（9464D）
ELOVL6-OE（9464D）
ELOVL6-SC（975A2）
ELOVL6-sh（975A2）
NK1.1
CD3
ELOVL6-Vector
ELOVL6-OE
ELOVL6-SC
ELOVL6-sh
ns
9464D
ns
975A2
0 2 4 6 8
NK1.1+ CD3- cells （%）

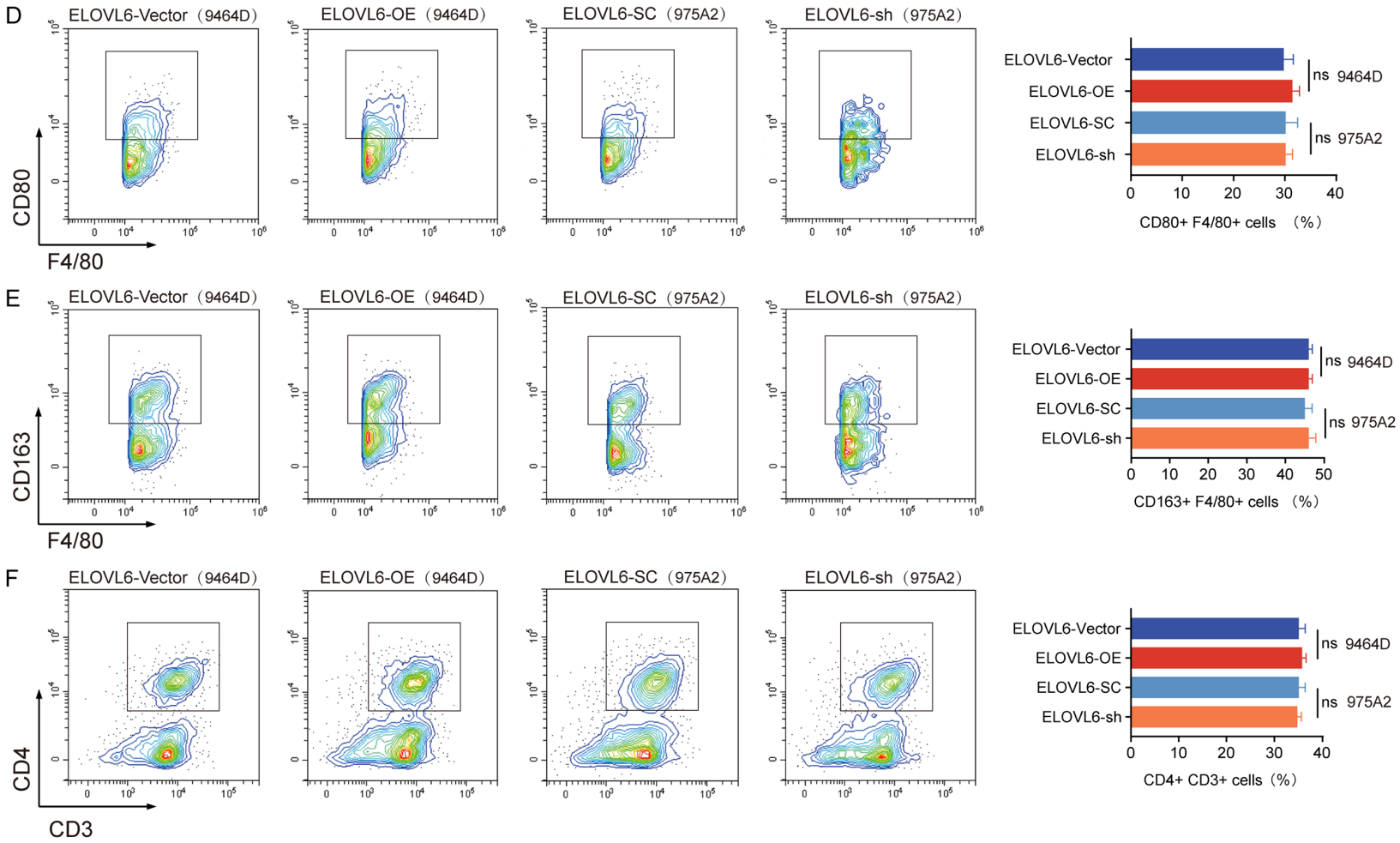

Figure S5. Effect of ELOVL6 expression on the immunosuppressive microenvironment of NB. (A-F) Flow cytometric analysis of harvested tumors: Representative dot plots and statistical analysis of the proportions of the exhausted T cells (PD1+ CD8; Tim3+ CD8 cells) (A, B). Representative dot plots and statistical analysis of the proportions of NK cells (C), M1 (Classical activated macrophages, CD80+ F4/80+) (D), M2 (Alternatively activated macrophages, CD163+ F4/80+) (E), and CD4+ T cells (F). Experiments were independently repeated thrice. Representative data are shown. Data are expressed as the mean ± standard deviation (SD). Paired and unpaired Student's t-tests were performed for in vitro and in vivo assays, respectively. n.s., no significant statistical difference; ***, $P < 0.001$; ****, $P < 0.0001$.

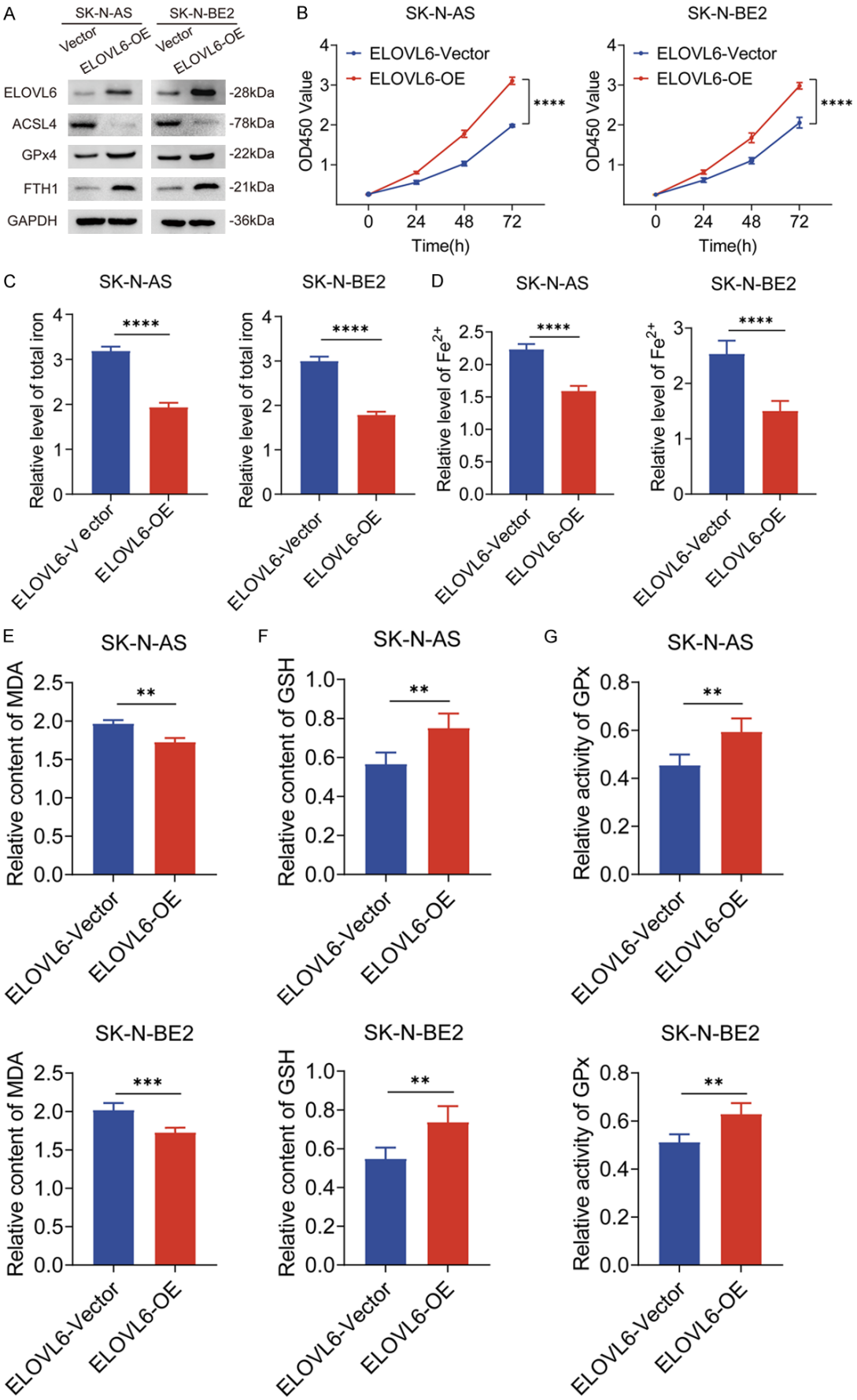
A
SK-N-AS
SK-N-BE2
Vector
ELOVL6-OE
Vector
ELOVL6-OE
ELOVL6
ACSL4
GPx4
FTH1
GAPDH
-28kDa
-78kDa
-22kDa
-21kDa
-36kDa
B
SK-N-AS
SK-N-BE2
ELOVL6-Vector
ELOVL6-OE
OD450 Value
Time(h)
****
C
SK-N-AS
SK-N-BE2
Relative level of total iron
ELOVL6-V ector
ELOVL6-Vector
ELOVL6-OE
D
SK-N-AS
SK-N-BE2
Relative level of Fe2+
E
SK-N-AS
SK-N-BE2
Relative content of MDA
**
***
F
SK-N-AS
SK-N-BE2
Relative content of GSH
G
SK-N-AS
SK-N-BE2
Relative activity of GPx

Figure S6. Overexpression of ELOVL6 inhibits ferroptosis in NB. (A) Western blot assay showed that overexpression of ELOVL6 inhibited ferroptosis in NB human cell lines (SK-N-AS and SK-N-BE2). (B) 24, 48, 72 h cell growth rates of NB human cell lines in the Vector and ELOVL6-OE groups were observed by CCK8 assay. (C, D) Total iron (C) and Fe^{2+} (D) in Vector and ELOVL6-OE groups were measured by iron detection assays. (E) Intracellular MDA in Vector and ELOVL6-OE groups was determined by MDA assays. (F) Intracellular GSH in Vector and ELOVL6-OE groups was determined by GSH assays. (G) Intracellular GPx in Vector and ELOVL6-OE groups was determined by GPx assays. Representative data are shown. Data are expressed as mean ± SD. Paired student's t test were performed for in vitro assays and unpaired student's t test were conducted for in vivo assays. n.s., no significant statistical difference; *, $P < 0.05$; **, $P < 0.01$; ***, $P < 0.001$; ****, $P < 0.0001$.